

***In situ* single particle classification reveals distinct 60S maturation intermediates in cells**

Bronwyn A. Lucas^{1,2,*}, Kexin Zhang^{1,2}, Sarah Loerch^{2,‡}, and Nikolaus Grigorieff^{1,2,*}

1. RNA Therapeutics Institute, University of Massachusetts Chan Medical School,
Worcester, MA, USA

2. Howard Hughes Medical Institute, Janelia Research Campus, Ashburn, VA, USA

*Correspondence: bronwyn.lucas@umassmed.edu, niko@grigorieff.org

‡Current address: Department of Chemistry and Biochemistry, University of California, Santa Cruz, CA, USA

Electron cryo-microscopy (cryo-EM) can generate high-resolution views of cells with faithful preservation of molecular structure. *In situ* cryo-EM, therefore, has enormous potential to reveal the atomic details of biological processes in their native context. However, in practice, the utility of *in situ* cryo-EM is limited by the difficulty of reliably locating and confidently identifying molecular targets (particles) and their conformational states in the crowded cellular environment. We recently showed that 2DTM, a fine-grained template-based search applied to cryo-EM micrographs, can localize particles in two-dimensional views of cells with high precision. Here we demonstrate that the signal-to-noise ratio (SNR) observed with 2DTM can be used to differentiate related complexes in focused ion beam (FIB)-milled cell sections. We apply this method in two contexts to locate and classify related intermediate states of 60S ribosome biogenesis in the *Saccharomyces cerevisiae* cell nucleus. In the first, we separate the nuclear pre-60S population from the cytoplasmic mature 60S population, using the subcellular localization to validate assignment. In the second, we show that relative 2DTM SNRs can be used to separate mixed populations of nuclear pre-60S that are not visually separable. We use a maximum likelihood approach to define the probability of each particle belonging to each class, thereby establishing a statistic to describe the confidence of our classification. Without the need to generate 3D reconstructions, 2DTM can be applied even when only a few target particles exist in a cell.

33 **Introduction:**

34 Locating and characterizing molecules in cells is an important goal of molecular,
35 structural, and cell biology. Cryogenic electron microscopy (cryo-EM) enables simultaneous
36 visualization of all cellular molecules in their native cellular environment while preserving high-
37 resolution molecular architecture. Therefore, cryo-EM holds the promise of delivering an
38 atomistic view of the cell. However, realizing this promise is limited by the high density of
39 molecules in a cell, making it difficult to identify molecules of interest (Lučić et al., 2013). As
40 one way to address this, electron cryo-tomography (cryo-ET) can be used to build 3D maps of
41 cellular structures in their native context (*in situ*) by constructing tomograms from a series of
42 tilted 2D images (Kürner et al., 2005; Lučić et al., 2013; Mahamid et al., 2016). In a tomogram,
43 molecules overlapping in any given view can be separated and large molecular assemblies
44 (particles) with distinctive shapes can be identified. Once identified, subtomogram averaging can
45 yield *in situ* molecular structures at <4 Å resolution (Himes and Zhang, 2018; Tegunov et al.,
46 2021). However, since the effective resolution of a raw tomogram is below 15-20 Å (Vilas et al.,
47 2020), identification of specific targets in tomograms is limited to abundant particles that are
48 sufficiently distinct at this resolution to be identified.

49 Many potential cell biological applications require accurate categorization of individual
50 molecule identity at a specific subcellular localization. Examples are the characterization of the
51 spatial organization of a biosynthetic process such as ribosome biogenesis, and the assignment of
52 molecular identities in small volumes such as synapses and vesicles. 3D classification of
53 subtomograms can differentiate between structural states (Himes and Zhang, 2018; Xue et al.,
54 2021). However, the assignment of states is unreliable for similar structures that can only be
55 distinguished using high-resolution detail, and statistical approaches to quantitatively assess
56 classification results are lacking. Machine learning has been employed for particle classification
57 in tomograms, but currently only performs as well as a human operator (Moebel et al., 2021).
58 While machine learning algorithms performed better than 3D template matching at molecule
59 localization in tomograms, classification remained challenging for all algorithms (Gubins et al.,
60 2020). *In situ* molecule classification, therefore, remains a major challenge.

61 We recently described an alternate method to locate particles that may improve structural
62 classification in cells. By using 2D cryo-EM images, rather than tomograms, and fine-grained,
63 high-resolution template matching (2DTM), specific particles can be located in cells with high

64 precision using their atomic structures (Lucas et al., 2021; Rickgauer et al., 2020, 2017). 2DTM
65 uses molecular models, from *in vitro* structure determination or *in silico* structure prediction
66 (e.g., Alphafold2 (Jumper et al., 2021)) to generate a 3D density. This 3D density (hereafter
67 referred to as the template) is then projected in 2D along millions of orientations. A pixel-wise
68 cross-correlation of the 2D projections with a high-resolution 2D cryo-EM image is performed,
69 yielding a 2DTM signal-to-noise ratio (SNR) at every pixel location (Rickgauer et al., 2017).
70 The 2DTM SNR values are subjected to a significance test, which identifies peaks with a desired
71 level of confidence (Lucas et al., 2021; Rickgauer et al., 2017). In the following, we refer to
72 targets passing this test as significant targets (Lucas et al., 2021; Rickgauer et al., 2017).

73 The 2DTM SNR is proportional to template mass and negatively affected by non-
74 matching elements between template and target (Lucas et al., 2021; Rickgauer et al., 2020,
75 2017). We have shown that a template generated from a *Bacillus subtilis* 50S large ribosomal
76 subunit was able to detect 50S in 2D cryo-EM images of *Mycoplasma pneumoniae* cells, but
77 with a lower average 2DTM SNR compared to a *M. pneumoniae* 50S template (Lucas et al.,
78 2021). This demonstrated that (1) 2DTM using partially matching templates can be sufficiently
79 sensitive to yield significant targets and (2) the mean 2DTM SNR of detected targets provides a
80 read-out of the relative similarity between different templates and populations of particle species.

81 In this study, we investigate whether the ratio of 2DTM SNRs obtained using different
82 templates can be used to identify the template that more closely resembles the cellular target, and
83 thereby classify particles in cells. As a model system, we chose to examine the late stages of 60S
84 ribosomal subunit biogenesis in the yeast *Saccharomyces cerevisiae* because (1) intermediates
85 are of a similar size and share significant structure with one another, making them difficult to
86 separate at low resolution, (2) molecular models spanning multiple late intermediate states have
87 recently been described, and (3) the maturation events that occur before and after nuclear export
88 have been characterized. Subcellular localization can thereby validate the assignment of
89 intermediate and mature states.

90 We show that 2DTM can locate and distinguish nuclear intermediates of 60S maturation
91 in 2D cryo-EM images of FIB-milled yeast cells. We confirm that 2DTM can distinguish
92 predefined 60S populations separated by subcellular localization and identify compositional
93 differences between them. We then applied a maximum likelihood-based approach to identify
94 two sub-populations of nuclear intermediates that were not otherwise separable and provide a

95 confidence of single particle classification. We show that using this approach, we can observe a
96 shift in the nuclear pre-60S intermediate population to a more mature intermediate after
97 inhibiting Crm1-mediated nuclear export. This study demonstrates that relative 2DTM SNR
98 ratios effectively distinguish related complexes and can identify changes to particle populations
99 in cells.

100

101 **Results:**

102 ***2DTM identifies 60S in biologically relevant locations and orientations in FIB-milled lamellae***

103 2DTM has been used to detect mammalian ribosomes in thin extensions of adherent cells
104 (Rickgauer et al., 2020), and bacterial ribosomes in *Mycoplasma pneumoniae* cells (Lucas et al.,
105 2021), both of which are sufficiently thin to permit imaging by transmission EM (TEM). Since
106 most eukaryotic cells are too thick to image by TEM, focused ion beam (FIB)-milling is used to
107 generate thin, electron transparent lamellae of cryogenically frozen cells (Marko et al., 2007;
108 Rigort et al., 2012; Villa et al., 2013).

109 To evaluate the utility of 2DTM to locate molecules in FIB-milled lamellae, we collected
110 28 2D cryo-EM images of the nuclear periphery of lamellae generated from actively growing
111 *Saccharomyces cerevisiae* cells (**Figure 1, Figure 1-figure supplement 1A-B**). We identified
112 4363 large ribosomal subunits by 2DTM using a template generated from a model representing
113 the mature 60S (PDB: 6Q8Y) (Tesina et al., 2019) (**Figure 1A-C**). The peaks corresponding to
114 significant detections were clearly distinguishable from background (**Figure 1E, Figure 1-figure**
115 **supplement 1C**), enabling precise localization of mature 60S in the cell.

116 To assess the specificity of 60S detection, we identified regions of the images
117 corresponding to the cytoplasm, nucleus and vacuole by visual inspection. Consistent with the
118 expected high specificity of 2DTM, we did not observe any significant mature 60S-detected
119 targets in regions of the image corresponding to the vacuole (**Figure 1C-D**). In contrast, 229
120 mature 60S-detected targets localized to the nucleus, representing ~5% of all mature 60S
121 identified targets in these images (**Figure 1C-D**). In regions of the images corresponding to the
122 cytoplasm we observe a median density of ~ 6500 60S/ μm^3 , which, assuming an average cell
123 volume of ~ 42 μm^3 of which $\sim 65\%$ is cytoplasm, corresponds to a total of $\sim 180,000$ 60S/cell
124 (**Figure 1G**). This is consistent with prior estimates of $187,000 \pm 56,000$ ribosomes per yeast
125 cell based on rRNA concentration (von der Haar, 2008).

126 Beyond the subcellular distribution of mature 60S-detected targets, we also confirmed
127 that 2DTM identified specific 60S in biologically relevant locations and orientations. The
128 nuclear envelope (NE) is contiguous with the endoplasmic reticulum and a known site for co-
129 translational transport of transmembrane and secretory proteins, while the vacuole is not known
130 to be a site of translation. We found that mature 60S-detected targets were oriented with their
131 polypeptide exit tunnels facing the cytoplasmic surface of the NE but were depleted from within
132 ~20 nm of the vacuole (**Figure 1C,F**). This indicates that the orientation of 60S identified by
133 2DTM is unlikely to be an artefact introduced by features of the membrane in the image. To
134 confirm that the targets identified with the mature 60S template reflect ribosomes, we generated
135 a 3D reconstruction using the locations and orientations of 3991 significant mature 60S-detected
136 targets using standard single particle approaches as described previously (Lucas et al., 2021). In
137 addition to the 60S the 10 Å-filtered reconstruction showed density consistent with the 40S small
138 ribosomal subunit (**Figure 1H**). This is consistent with many of the mature 60S detected targets
139 representing a population of 80S ribosomes. We conclude that 2DTM-identified locations and
140 orientations in 2D cryo-EM images of FIB-milled lamellae reflect biologically relevant locations
141 and orientations of ribosomes in the cell.

142

143 *Relative 2DTM SNRs enable single particle classification in situ*

144 The nuclear envelope (NE) creates a physical barrier that separates premature 60S in the
145 nucleus from mature 60S in the cytoplasm and is easily distinguishable in many 2D images by its
146 characteristic double membrane and by the more granular appearance of the cytoplasm vs the
147 nucleus (e.g., **Figure 1B**). Our observation of a substantial population of mature 60S-detected
148 targets in the nucleus, but not in the vacuole (**Figure 1C-D**), suggests that the nuclear 60S may
149 result from cross-detection of nuclear precursors, which share part of their structure with mature
150 60S and therefore also produce significant correlations (**Figure 2A**). As a first step to
151 differentiate between related 60S intermediates, we located precursor 60S by 2DTM searches
152 using a template generated from a late nuclear intermediate (LN 60S, PDB: 6N8J) (Zhou et al.,
153 2019) (**Figure 2A,B**), and annotated each target by its subcellular localization. The LN 60S was
154 chosen because it represents the most mature nuclear intermediate for which there is a structure,
155 and which retains ribosome biogenesis factors (RBFs) that are removed during nuclear and early
156 cytoplasmic processing (**Figure 2A**). Thus, we expect that (1) the similarities between the

157 mature 60S and LN 60S structures will result in cross-detection of the respective other complex
158 and (2) the cytoplasmic population will more closely resemble the mature 60S and nuclear
159 population will more closely resemble the LN 60S resulting in a higher mature 60S / LN 60S
160 2DTM SNR ratio in the cytoplasm than the nucleus. In the 28 images of the nucleus and nuclear
161 periphery we located 1651 significant LN 60S-detected targets of which 1382 (~84%) of the LN
162 60S-detected targets were cytoplasmic and 268 (16%) were nuclear (**Figure 2-figure**
163 **supplement 1A**). We identified more cytoplasmic than nuclear targets in 2DTM searches with
164 both mature and LN 60S templates because (1) the cytoplasm represented a larger area of our
165 images and (2) the concentration of 60S is expected to be higher in the cytoplasm relative to the
166 nucleus (e.g., (Delavoie et al., 2019)). Only one of the significant LN 60S-detected targets
167 localized to the vacuole, which is below the expected false positive rate and further indicates the
168 specificity of 2DTM.

169 As expected from the similarity between the mature and LN 60S templates, the locations
170 of many of the targets identified in the two searches overlap (**Figure 2B,C**). We aligned the two
171 sets of coordinates using the program *align_coordinates* (Lucas et al., 2021). Approximately one
172 third of the mature 60S-detected targets overlapped with LN 60S-detected targets while 92% of
173 the LN 60S-detected targets overlapped with mature 60S-detected targets (**Figure 2H**).
174 Combining the results of both searches, only 0.5% of the cytoplasmic targets were LN 60S-
175 detected only, compared to 30% of the nuclear targets (**Figure 2I**).

176 Consistent with their expected localizations, the median $\log_2(\text{mature 60S} / \text{LN 60S}$
177 2DTM SNR) values

178 of targets identified with both templates were significantly higher for the cytoplasmic
179 population than the nuclear population ($p < 0.0001$, K-S. test) (**Figure 2D-G,J**). We classified
180 each target as LN or mature 60S according to the highest 2DTM SNR (**Figure 1K**). Of the
181 population detected with both mature and LN 60S templates, 94% of the 1361 cytoplasmic
182 targets have a closer match (higher SNR) with the mature 60S and 88% of the 171 nuclear
183 targets have a closer match with the LN 60S (**Figure 1J**). Combining all 60S-detected targets,
184 the nuclear 60S targets are now more clearly distinguished from the cytoplasmic population with
185 98% of the cytoplasmic targets annotated as mature 60S, and 60% of the nuclear targets
186 annotated as pre-60S (**Figure 1K,L**). The ~40% of nuclear targets that more closely resemble the
187 mature 60S likely reflect nuclear intermediates different from the LN 60S (see below) and thus

188 do not perfectly match either template. We conclude that comparing 2DTM SNRs can effectively
189 differentiate populations of related particles *in situ*.

190

191 ***Defining a confidence metric for single particle classification in situ***

192 To gain an understanding of cell biology at molecular resolution it is necessary to be able
193 to confidently assign particle identity to individual targets. We show above that the nuclear and
194 cytoplasmic 60S populations were significantly different with respect to their relative similarity
195 to the LN and mature 60S (**Figure 2**). We also show that classifying targets by their highest
196 2DTM SNR effectively separates the nuclear from the cytoplasmic population (**Figure 2**).
197 However, a single threshold does not fully capture the differences between the nuclear and
198 cytoplasmic populations and for an individual particle the confidence of classification is unclear.

199 To assign a confidence in the class assignments of detected particles we developed a
200 maximum likelihood-based approach to infer the probability of a particle deriving from one of a
201 given number of populations. We sought to classify each of the 1531 LN and mature 60S-
202 detected targets by their relative similarity to the LN 60S or mature 60S templates. We restricted
203 our analysis to the targets that were detected by both templates to limit the contribution from
204 noise. We made the initial simplifying assumption that: 1) each 60S identified more closely
205 reflects either LN or mature 60S, i.e., the number of classes needed to describe all detected
206 targets is two; 2) the nuclear targets more closely resemble the LN 60S and the cytoplasmic
207 targets more closely resemble the mature 60S. We therefore define the prior probability that a
208 randomly selected detected target belongs to a specific population according to the number of
209 targets detected in the nucleus and cytoplasm, respectively (**Figure 2J, Figure 2-figure**
210 **supplement 1A**):

211 $P(\text{targets being LN 60S}) = P(\text{Nucleus}) = 0.11$ and

212 $P(\text{targets being mature 60S}) = p(\text{Cytoplasm}) = 0.89$.

213 We used a maximum likelihood-based approach to model the $\log_2(\text{mature} / \text{LN 60S})$
214 2DTM SNR) values as a mixture of two Gaussians (**Figure 3A**, $R^2 = 0.993$). The fit suggests a
215 major population that more closely reflected the mature 60S and a smaller population that more
216 closely reflected the LN 60S (**Figure 3A**). Using the Gaussian distribution model (see Materials
217 and Methods), we calculate the probability that a LN and mature 60S-detected target with a
218 given $\log_2(\text{mature} / \text{LN 60S SNR})$ value more closely resembles the LN 60S than the mature 60S

219 via Bayes rule (**Figure 3B-C**). This analysis could easily be extended to cases where more than
220 two templates are used in the search (see Materials and Methods). A confidence threshold of
221 95% assigns 27% of the nuclear targets and only ~0.2% of the cytoplasmic targets to the LN 60S
222 population (**Figure 3C**). Defining a threshold at 50% classifies ~75% of the nuclear targets as
223 LN 60S and 92% of the cytoplasmic targets as mature 60S (**Figure 3C**). The relative probability
224 of each detected 60S belonging either to the LN or mature 60S population can be readily
225 visualized (**Figure 3D**). This shows that the 2DTM SNR ratio can effectively delineate
226 populations of related particles in cells with a specified confidence for each particle assignment.
227

228 *Ribosome biogenesis factors differentiate nuclear from cytoplasmic 60S*

229 Most of the mass difference between the LN and mature 60S templates results from
230 proteins in the LN 60S that are absent in the mature 60S (**Figure 4A-C**). Notable exceptions are
231 the proteins on the P-stalk are present only on the mature 60S (**Figure 4A-C, Figure 3A**).
232 Additionally, several rRNA helices on the intersubunit interface are in different conformations,
233 specifically the L1 stalk, helix 38 and helix 89, which undergo conformational changes during
234 maturation (**Figure 4C**). To identify which of these features distinguish nuclear from
235 cytoplasmic 60S, we investigated the relative dependence of the 2DTM SNRs on the rRNA and
236 proteins of the LN 60S template. We generated truncated LN 60S templates containing either
237 rRNA or protein only and calculated the change in the 2DTM SNR for each template at each
238 target relative to the full-length template (**Figure 4D**). The rRNA contributed 1.5 and 1.8-fold
239 more to the 2DTM SNR of the nuclear and cytoplasmic targets, respectively, despite comprising
240 only 1.25-fold more of the template mass (1004 and 800 kDa, respectively), than the proteins
241 (**Figure 4D**). Indeed, 60% of the cytoplasmic targets and 34% of the nuclear targets were no
242 longer significant when searching with the proteins alone. Comparing the nuclear and
243 cytoplasmic populations shows that the 2DTM SNR of the LN 60S-detected cytoplasmic targets
244 is less affected by the removal of the LN 60S proteins and more strongly affected by the removal
245 of the rRNA (**Figure 4D**). This shows that the LN 60S proteins contribute more to the SNR of
246 the nuclear targets than the cytoplasmic targets and are therefore more effective at differentiating
247 the nuclear from the cytoplasmic 60S population.

248 Since the LN 60S represents a late intermediate of 60S maturation in which the rRNA is
249 almost fully folded, RBF proteins on the LN 60S account for most of the difference with the

250 mature 60S by mass (**Figure 4A-D**). To confirm that the SNR difference of nuclear LN 60S-
251 detected targets and cytoplasmic mature 60S-detected targets is primarily due to the RBF
252 proteins, we removed the RBFs from the LN 60S template and recalculated the SNR for each
253 target. The removal increased the 2DTM SNR ratio of the cytoplasmic targets, while decreasing
254 the 2DTM SNR of the nuclear targets (**Figure 4E**), making the SNR values more similar. This is
255 consistent with the nuclear population having these RBFs and the cytoplasmic population lacking
256 the RBFs. We conclude that the differentiation of detected targets using the observed 2DTM
257 SNRs reflects biologically relevant differences between them.

258

259 *Nog2 lacking intermediates accumulate after inhibition of nuclear export*

260 The two largest RBFs on the LN 60S are Nog1 and Nog2, together accounting for ~50%
261 of the RBF mass (**Figure 4F,G**). During 60S maturation, Nog2 removal is required to permit
262 binding of the nuclear export adaptor Nmd3 and Crm1-dependent export, and therefore Nog2
263 removal precedes nuclear export (Ho et al., 2000; Matsuo et al., 2014). In contrast, Nog1 is
264 removed only upon export to the cytoplasm (Pertschy et al., 2007). In cells with active nuclear
265 export, we find that removal of either Nog1 or Nog2 differentiates the nuclear from the
266 cytoplasmic populations (**Figure 4F,G**, untreated cells). As a further test of differentiating
267 different targets by 2DTM, we inhibited Crm1 mediated export by treating Leptomycin B (LepB)
268 sensitive Crm1 (T539C) cells with LepB and located 60S targets with LN 60S and mature 60S
269 templates in eight images of FIB-milled lamellae. To assess the relative occupancy of Nog1 and
270 Nog2 after Crm1 inhibition, we measured the change in 2DTM SNR after removal of all RBFs,
271 and Nog1 or Nog2 alone. Consistent with LepB inhibiting export of pre-60S from the nucleus,
272 we detected a higher density of pre-60S in the nucleus than in cells with active Crm1 (**Figure 4-**
273 **figure supplement 1A**). When nuclear export is inhibited, all RBFs (**Figure 4E**) and Nog1 alone
274 (**Figure 4F**) still differentiate the nuclear from the cytoplasmic populations. In contrast, the
275 occupancy of Nog2 is no longer significantly different between the nuclear and cytoplasmic
276 populations (**Figure 4G**). This is consistent with a model in which, when Crm1-mediated export
277 is active, nuclear intermediates are rapidly exported after removal of Nog2, depleting the Nog2-
278 lacking population from the nucleus. In the presence of a Crm1-inhibitor, the late, export
279 competent nuclear intermediate lacking Nog2 can no longer be exported and therefore
280 accumulates. Since Nog1 is only removed after export, inhibition of export did not change the

281 occupancy of Nog1 on the maturing 60S. This demonstrates that comparing 2DTM SNRs is
282 sufficiently sensitive to assess the occupancy of individual proteins *in situ*.

283

284 ***Classification of nuclear pre-60S intermediates***

285 Ribosome biogenesis is a highly efficient molecular assembly line, and multiple
286 intermediate states co-exist in the cell (Warner, 1999). Therefore, the nuclear population of pre-
287 60S is unlikely to represent a single intermediate population. Accordingly, the distribution of the
288 mature 60S / LN 60S SNR ratios of nuclear mature and LN 60S-detected targets fits a single
289 Gaussian more poorly than the cytoplasmic targets (**Figure 2J**), suggesting that additional
290 nuclear populations were identified with both 60S templates. To test this prediction and
291 investigate the nuclear pre-60S population further, we generated a third template corresponding
292 to an earlier nuclear intermediate (EN 60S). EN 60S (PDB: 3JCT) retains internally transcribed
293 spacer RNA 2 (ITS2) and associated proteins and has 5S rRNP in a premature state rotated 180°
294 relative to the LN and mature 60S (**Figure 5A**) (Wu et al., 2016). We identified 679 significant
295 EN 60S-detected targets of which 545 (~80%) were also identified with the LN 60S template,
296 and 489 (72%) were also identified with the mature 60S. All of the 489 EN 60S-detected targets
297 identified with the mature 60S were also identified with the LN 60S (**Figure 5A**). 289 (43%) of
298 the EN 60S-detected targets localized to regions of the images corresponding to the nucleus,
299 similar to the 268 nuclear LN 60S-detected targets, while only 390 were cytoplasmic, >3-fold
300 fewer than located with the LN 60S template, consistent with the EN 60S representing a less
301 mature nuclear intermediate (**Figure 5B**). The number and localization of targets identified with
302 2DTM is consistent with their sequence in the maturation pathway, progressing from EN 60S to
303 LN 60S in the nucleus to mature 60S in the cytoplasm.

304 Cross-detection of targets by different templates can be used to detect heterogeneity in
305 target populations. When examining the SNR ratios of targets identified by both EN and LN 60S,
306 the cytoplasmic targets display a distribution that is consistent with a single population that more
307 closely resemble the LN 60S template (**Figure 5-figure supplement 1B, red**). The distribution
308 of nuclear targets, however, was consistent with at least two populations (**Figure 5-figure
309 supplement 1B, blue**), each of which is distinct from the cytoplasmic population. This indicated
310 the presence of at least two nuclear populations that differ with respect to their relative similarity
311 to the EN and LN 60S templates.

312 We next sought to classify the EN, LN and mature 60S-detected targets based on their
313 relative similarity to the three 60S templates. For each target we calculated the $\log_2(\text{mature 60S} /$
314 $\text{LN 60S SNR})$ and $\log_2(\text{EN 60S} / \text{LN 60S SNR})$ values. We used these values to classify each
315 target based on the relative similarity to the three templates using the maximum-likelihood
316 approach discussed above (**Figure 5C**). We found that, consistent with their expected subcellular
317 distributions, targets assigned to the mature 60S population represented 315 (85%) of the
318 cytoplasmic targets and only 1 (<1%) of the nuclear targets detected by all three templates
319 (**Figure 5D**). In contrast, the EN 60S population represents 83 (70%) of the nuclear population
320 and only 4 (~1%) of the cytoplasmic population detected with all three templates (**Figure 5D**).
321 The LN 60S population was roughly evenly distributed between the nucleus and the cytoplasm,
322 consistent with this structure representing a late maturation intermediate (**Figure 5D**).

323 The NE provides a convenient visual control for the classification of targets as LN / EN
324 60S or mature 60S (e.g., **Figure 1**). However, there are no clear features in the nucleoplasm that
325 would enable visual separation of different populations of nuclear intermediates and thereby
326 confirm their classification. To validate our classification of the nuclear pre-60S populations, we
327 identified conditions wherein the relative occupancy of the two states would be expected to
328 change. We show above that inhibiting Crm1-mediated export results in accumulation of nuclear
329 intermediates that lack Nog2 (**Figure 4**). In cells with active Crm1, 57% of the nuclear 60S
330 targets are assigned to the EN 60S population (**Figure 5E**). After inhibition of Crm1-mediated
331 export, the EN 60S population is mostly depleted, and >90% of targets are assigned to the LN
332 60S population (**Figure 5E**). This confirms that 2DTM SNR ratios can be used to effectively
333 classify mixed populations of particles in cells.

334

335 **Discussion:**

336 The immense potential for cryo-EM to reveal the molecular detail of biological processes
337 in cells is currently largely unrealized. One of the major bottlenecks is the lack of reliable,
338 quantitative methods to locate and characterize molecules in cells. Here we describe the
339 application of 2DTM to *in situ* particle classification. By considering the relative 2DTM SNRs of
340 alternate templates at a single location and orientation, we separate 60S precursors in the nucleus
341 from mature 60S in the cytoplasm. We also show that a maximum likelihood approach
342 effectively classifies a mixed population of nuclear pre-60S into at least two maturation states

343 with a specified confidence for each particle. We show that 2DTM can be used to probe the
344 composition of complexes *in situ* by modifying 2DTM templates. In this study we extend the
345 utility of 2DTM beyond a binary indicator of detection to provide a quantitative assessment of
346 particle identity.

347

348 ***2DTM enables specific molecule localization in the dense interior of cells***

349 Cryo-FIB milled eukaryotic cells are sufficiently well preserved to allow imaging with
350 cryo-ET (Mahamid et al., 2016) and subtomogram averaging to yield 3D reconstructions at
351 resolutions of $>\sim 12\text{\AA}$, e.g., (Schaffer et al., 2019). However, before the present work it was
352 unclear if the milling preserves the high-resolution signal in these samples sufficiently well to
353 allow for particle detection with 2DTM. Our results clearly show that FIB-milling is compatible
354 with molecule localization by 2DTM. This expands the application of 2DTM to previously
355 inaccessible cell types and further demonstrates the utility of 2DTM for *in situ* structural biology.

356 In many images, 60S subunits detected by 2DTM also generate low-resolution contrast in
357 the cytoplasm that is readily visible (**Figure 1B**, yellow arrows). In the nucleoplasm, the similar
358 density of RNA and DNA impedes the visual identification of all but a few pre-60S (**Figure 1B**,
359 blue arrows). However, the reduced low-resolution contrast does not preclude effective detection
360 of pre-60S with 2DTM. This is in contrast to particle localization in tomograms, wherein
361 detection depends more strongly on low-resolution contrast and recognizable shapes. The ability
362 to distinguish particles in crowded molecular environments is a major advantage of 2DTM
363 relative to cryo-ET, which currently suffers from strong attenuation of high-resolution signal
364 (large B-factors) in the raw tomogram (Schur et al., 2016). 2DTM may enable localization of
365 molecules in other dense environments such as liquid-liquid phase separated granules, which
366 remains challenging for cryo-ET despite success in some cases (Erdmann et al., 2021). Our
367 results confirm that 2DTM is an effective method to localize molecules in dense regions of the
368 cell even when the molecules cannot be distinguished by eye.

369

370 ***2DTM enables single particle classification in situ***

371 In previous work we and others have demonstrated that, when comparing populations of
372 molecules, the average 2DTM SNRs reflect the relative similarity of different templates to the
373 target populations (Lucas et al., 2021; Rickgauer et al., 2020). In this study, we extend this

374 observation to show that the relative 2DTM SNRs of aligned templates *at a specific location and*
375 *orientation* can be used to calculate the relative probabilities of a target belonging to a specific
376 particle population.

377 Of the nuclear targets identified with the mature 60S, ~50% were also detected with the EN
378 60S, all of which were also detected with the LN 60S (**Figure 5B**). When calculating the relative
379 similarity to the three 60S templates, the EN 60S and mature 60S population were clearly
380 distinct, with mean 2DTM SNR ratios more than three standard deviations apart (**Figure 5C**).
381 The maximum likelihood estimation of Gaussian distributions enables quantitative classification
382 even when particle populations are less distinct, by yielding relative probabilities for each
383 detected target belonging to one of a given number of populations (e.g., **Figures 3&5**).

384 In this study, we effectively classify at least three populations of 60S maturation states from a
385 population of <500 molecules (**Figure 5**). This means that given sufficient abundance of the
386 target, it will be possible to distinguish populations based on data from a single image (**Figure 2-**
387 **figure supplement 1D**). This contrasts with more traditional (reference-free) methods used to
388 classify subtomograms and single particles, which require hundreds to thousands of particles to
389 generate the class averages needed for particle assignment. 2DTM allows single molecule
390 classification from fewer images, and therefore enables more information to be extracted from
391 images collected from cells and purified samples (single-particle cryo-EM).

392

393 ***Confidence metric for single particle classification in situ***

394 Calculating the confidence in class assignment of individual particles will aid interpretation
395 of the results of 2DTM *in situ*. One major difference between *in situ* cryo-EM and single-particle
396 cryo-EM is the type of biological information that is obtained. In single-particle cryo-EM, the
397 goal is to generate high-resolution maps and establish the arrangement of atoms within a
398 complex in different functional states, and to use this information to discern its molecular
399 mechanism. In this case, B-factors and other metrics can be used to indicate uncertainty about an
400 atomic coordinate, which aids interpretation of the model built into the map. In the cell, each
401 individual instance of a complex may be in a different context relative to other similar molecules.
402 For example, particles might be in different subcellular compartments such as the nucleus or
403 cytoplasm or, as a more extreme example, a single particle within a nuclear pore exists in a very
404 different context than particles in the nucleoplasm. For structural cell biology applications,

405 therefore, it is useful to define a metric to establish the confidence of single particle
406 classification. In this study, we show that a maximum likelihood approach using Gaussian fits to
407 \log_2 2DTM SNR ratios of alternate templates at a specific subcellular location and orientation
408 can be used to calculate the relative probability of a single particle deriving from one of a given
409 number of classes. This provides a quantitative metric to establish confidence in the assignment
410 of single particles that will aid in the biological interpretation of cellular cryo-EM maps.

411

412 ***2DTM templates as computational molecular probes***

413 A major challenge in biological cryo-EM the retrieval of detailed structural information of
414 inherently flexible and heterogeneous macromolecules from noisy images collected at low dose
415 to limit radiation damage. In single particle cryo-EM, this problem is addressed by averaging
416 images of thousands of purified molecules to identify different structural states at high
417 resolution. By averaging images of many identical copies of a particle, novel structures can be
418 discovered, and this is a clear strength of this approach. However, since most complexes have a
419 low abundance in the cell, the utility of this approach for *in situ* structural biology is limited to
420 all but the most abundant complexes.

421 2DTM presents an alternate approach to using the signal in noisy images to gain insight into
422 the structural states of molecules. In this approach, a noise-free template represents a hypothesis
423 that a particle of a given conformational and compositional state is present in the image, and this
424 hypothesis can be tested by searching the image with the template, independent of how many
425 particles the image contains. We demonstrate that by generating modified templates representing
426 different hypotheses, we can directly assess the compositional and conformational states of
427 ribosomal subunits in cells.

428 Provided the templates have similar molecular mass and shape and are aligned with each
429 other, probing with multiple templates requires only a single initial exhaustive search with one of
430 the templates. This can be followed by a simple evaluation of the cross-correlation coefficient for
431 each additional template at locations and orientations of the detected targets in the initial search
432 (**Figure 4**), thereby avoiding time-consuming searches for all templates. In future studies, this
433 approach could be extended to assess the relative similarity of a target with respect to a library of
434 alternate structures. Alternate templates could be generated in multiple ways, depending on the
435 biological hypothesis being tested. To reveal compositional heterogeneity *in situ*, alternate

436 structures could be generated that lack specific subunits of interest as shown in **Figure 4**.
437 Additionally, to interrogate *in situ* conformational heterogeneity, templates could be generated
438 from time points of molecular dynamics simulations.

439

440 ***Addressing potential sources of error***

441 In our study, we used the physical separation of nuclear and cytoplasmic 60S populations
442 to develop and test *in situ* classification of targets by 2DTM. We found that there are several
443 requirements to permit classification of related molecules by 2DTM. First, the molecular models
444 must be aligned relative to one another resulting in a correlation peak at the same pixel in the
445 image. Comparing SNR values resulting from global searches with different templates may be
446 lowered by imperfect, off-grid rotational matches, potentially affecting 2DTM SNR ratios and
447 hence, target classification. Differences in model quality may also affect the 2DTM SNR ratios,
448 masking other differences of interest. In this study, the mature 60S template was generated using
449 the atomic coordinates of the large subunit of the ribosome built into a map with an overall
450 resolution of 3.1 Å (PDB: 6Q8Y) (Tesina et al., 2019). The large subunit of the ribosome is
451 structurally less variable than the small subunit and local resolution estimates suggest that parts
452 of the LSU map extend to ~2.5 Å (Tesina et al., 2019). The maps used to build the EN 60S and
453 LN 60S subunits were reconstructed at 3.08 Å and at 3.5 Å resolution, respectively. The
454 accuracy of the atomic coordinates of a model will depend on the resolution of the underlying
455 density map. Moreover, the greater number of mature ribosome structures, relative to maturation
456 intermediate structures, may provide more confidence in the atomic coordinates of the mature
457 60S. We expect that more accurate coordinates will result in higher 2DTM SNR values, which
458 may affect target classification.

459 The dependence of 2DTM SNR values on the quality of the atomic model presents the
460 possibility to use 2DTM to refine atomic models directly against 2D images of purified samples,
461 and *in situ* against targets detected in images of cells. This approach may bypass some of the
462 difficulties associated with the use of intermediary 3D reconstructions in atomic model
463 refinement, such as inaccurate representation of the full extent of heterogeneity in a dataset and
464 loss of resolution in flexible parts of a molecule. Further development is required to address the
465 potential of overfitting when refining against noisy 2D images, and to detect and quantify errors
466 in the refined models.

467 The classification of structurally similar targets could be further improved by identifying
468 and controlling the factors that affect the distribution of observed 2DTM SNR ratios for a given
469 set of templates. Ideally, the mean ratio of SNR values for a set of templates and given target
470 depends only on the structural differences between the templates, while the distribution of
471 observed ratios is solely a function of the noise and background in the images. However, factors
472 that contribute to loss of signal such as sample thickness, radiation damage, beam induced
473 motion, charging and movie frame alignment errors due to sample deformation all result in loss
474 of high-resolution signal, making the 2DTM SNR ratios less sensitive to structural differences in
475 the templates and biasing their \log_2 values towards 0. Additionally, structural variability in the
476 targets that is not captured by the templates, as well as different degrees of overfitting during
477 2DTM (Lucas et al., 2021) and a target orientation dependence of the SNR values may lead to a
478 wider spread of observed 2DTM SNR ratios. Further research is required to account for these
479 factors and reduce the variance in 2DTM SNR ratios, thereby enabling classification of targets
480 with smaller structural differences.

481

482 ***Additional intermediate populations***

483 In the present study, we only considered three alternate 60S templates. We note that the
484 Gaussian fits to the 2DTM SNRs of mature 60S and LN 60S-detected nuclear targets is
485 imperfect, potentially indicating additional pre-60S populations (**Figure 2-figure supplement**
486 **1C**). Further examination of the observed 2DTM SNR ratios revealed the presence of at least one
487 additional pre-60S population (**Figure 5**). We also observed a small population of cytoplasmic
488 60S targets with higher SNR values against the LN 60S template than against the mature 60S
489 (**Figure 5D**). 60S maturation intermediates exit the nucleus in an immature form and complete
490 maturation in the cytoplasm. Whether the cytoplasmic 60S with higher SNR values against the
491 LN 60S template represent cytoplasmic intermediates or reflect the limits of our classification
492 strategy requires further investigation. Future work using additional templates representing other
493 intermediates of 60S maturation will reveal further details about the spatiotemporal organization
494 of pre-60S intermediates in cells.

495 In this study, we identified an EN 60S population of nuclear 60S with the 5S rRNP in a
496 premature state rotated 180° relative to the mature 60S, consistent with *in vitro* determined
497 structures (Leidig et al., 2014). The presence of this complex during maturation *in vivo* has been

498 difficult to establish. Our observation that this population accounts for more than half of the 60S
499 identified in the nucleus argues that this is an on-pathway assembly intermediate. We also
500 identified a nuclear LN 60S population. This population reflects a late intermediate that has
501 already undergone 5S rotation and ITS2 removal, implying a temporal lag after 5S rotation
502 and/or ITS2 removal, and subsequent export from the nucleus. To test these possibilities more
503 thoroughly, future studies establishing the flux through the assembly pathway are needed. By
504 freezing cells at different time points after inhibition of specific maturation steps, 2DTM could
505 be used to study the kinetics of assembly and the flux through the assembly pathway.

506

507 **Materials and Methods:**

508 *Yeast cell culture and plunge freezing*

509 *Saccharomyces cerevisiae* strains BY4741 (ATCC), or MNY8 (a gift from Michael Rosbash)
510 colonies were inoculated in 20mL of YPD, diluted 1/5 and grown overnight to an OD₆₀₀ of ~0.5
511 to 1. The cells were then diluted to 10,000 cells/mL and 3 μ L applied to a 2/1 or 2/2 Quantifoil
512 200 mesh Cu grid, allowed to rest for 15 seconds, back-side blotted for 8 seconds and plunged
513 into liquid ethane at -184°C using a Leica EM GP2 plunger. Frozen grids were stored in liquid
514 nitrogen until FIB-milled. When indicated Crm1(T539C) (MNY8 cells, a gift from Michael
515 Rosbash, Brandeis) were additionally incubated at 30°C with shaking in the presence of 200 nM
516 Leptomycin B (Cell Signaling Technologies) for 30 min before applying to grids and plunge
517 freezing.

518

519 *FIB milling*

520 Grids were transferred to an Aquilos cryo-FIB SEM, sputter coated with metallic Pt for 15s then
521 coated with organo-Pt for 10s and milled in a series of sequential milling steps using a 30kV Ga⁺
522 beam using the following protocol: rough milling 1: 0.1 nA rough milling 2: 50 pA lamella
523 polishing: 10 or 30 pA at a stage tilt of 15° (milling angle of 8°).

524

525 *Cryo-EM data collection*

526 Lamellae were imaged using a Titan Krios 300 keV cryo-TEM (Thermo Fisher) equipped with a
527 K3 direct detector (Gatan) and an energy filter (Gatan) at a sample pixel size of 1.06 Å. Movies
528 were collected at an exposure rate of 1 e⁻/Å² to a total dose of 30 e⁻/Å².

529

530 ***Image processing***

531 Images were processed using *cis*TEM (Grant et al., 2018) as described previously (Lucas et al.,
532 2021), and using sample tilt determination implemented in a modified version of CTFFIND4
533 (Rohou and Grigorieff, 2015) to estimate sample defocus to account for the $\sim 8^\circ$ tilt of the lamella
534 introduced during FIB-milling. Images of 3D densities and 2DTM results were prepared in
535 ChimeraX (Pettersen et al., 2021).

536

537 ***2DTM***

538 The molecular models noted in the text were aligned to one another to have the same origin
539 using their 28S rRNA using the MatchMaker function in UCSF Chimera (Meng et al., 2006;
540 Pettersen et al., 2004) and 2DTM templates were generated by simulating 3D densities (Himes
541 and Grigorieff, 2021). 2DTM was performed using the program *match_template* in the *cis*TEM
542 GUI (Lucas et al., 2021) using the default parameters. The coordinates were refined using the
543 program *refine_template* (Lucas et al., 2021) in rotational steps of 0.1° and a defocus range of
544 200\AA with a 10\AA step.

545

546 ***3D reconstruction using mature 60S 2DTM coordinates***

547 We used the program *prepare_stack_matchtemplate* (Lucas et al., 2021) to generate a particle
548 stack using the locations and orientations of the significant mature 60S-detected targets after
549 refinement as described above. We then used *cis*TEM to generate a 3D reconstruction from 3991
550 mature 60S targets detected in 28 images of the nuclear periphery, only including targets with a
551 2DTM SNR of >8 . The reconstruction had a nominal resolution of 3.5\AA using an Fourier Shell
552 Correlation (FSC) threshold of 0.143 (**Figure 1-figure supplement 1D**) (Rosenthal and
553 Henderson, 2003) that is expected to overestimate the resolution due to overfitting (Lucas et al.,
554 2021). To limit the noise due to overfitting, we low-pass filtered the reconstruction to 10\AA ,
555 representing an FSC of 0.9.

556

557 ***Calculating 2DTM SNR values and ratios of SNR values***

558 Targets identified in two or more searches with aligned templates were identified using the
559 program *align_coordinates* (Lucas et al., 2021). The 2DTM SNRs of targets identified in two or

560 more searches were compared by taking the \log_2 of the SNR ratio. The \log_2 was used in place of
 561 the direct ratio because, the shape of the distribution is independent of the order of comparison,
 562 except for a mirror around 0, while the distribution of the direct ratios shows more complicated
 563 behavior. Histograms of both the \log_2 values and direct ratios of the cytoplasmic 60S population
 564 have approximately Gaussian distributions with fits characterized by the coefficient of
 565 determination $R^2=0.993$ and $R^2=0.991$ respectively. To calculate the change in the 2DTM SNR
 566 with modified templates, the program *refine_template* (Lucas et al., 2021) was used to calculate
 567 2DTM SNRs for additional templates using the locations and orientations from a previous
 568 exhaustive search with an initial template, without performing a rotational search by specifying
 569 the rotational step as 360° . To obtain consistent ratios of 2DTM SNRs, the 2DTM SNR values
 570 for both the initial template and the additional templates were calculated.

571

572 *Calculating relative probabilities*

573 Histograms were generated (bin 0.05) of the calculated \log_2 2DTM SNR ratios and Gaussians
 574 were fitted using GaussianMixture in sklearn (Pedregosa et al., 2011). Based on the shape of the
 575 histogram, we model the \log_2 2DTM SNR ratios as a mixture of K -component multivariate
 576 Gaussian distributions, when K templates are used in the search. We fit Gaussians to the \log_2
 577 SNR ratios of any two selected templates. Each target i is then associated with $K - 1$ such SNR
 578 ratios x_i . For example, for $K = 4$, we can define the following:

579

$$580 \quad X_i = \begin{bmatrix} \log_2(SNR_{i,k=1}/SNR_{i,k=2}) \\ \log_2(SNR_{i,k=1}/SNR_{i,k=3}) \\ \log_2(SNR_{i,k=1}/SNR_{i,k=4}) \end{bmatrix} \quad (1)$$

581

582 For particles belonging to the same population (class), the \log_2 SNR ratio can be described by the
 583 multivariate Gaussian probability density function (PDF):

584

$$585 \quad P(X_i|\Theta_k, z_i = k) \sim \mathbb{N}(M_k, \Sigma_k) = \frac{1}{(2\pi)^{\frac{d}{2}}|\Sigma_k|^{\frac{1}{2}}} \exp\left(-\frac{(X_i-M_k)^T \Sigma_k^{-1} (X_i-M_k)}{2}\right) \quad (2)$$

586

$$587 \quad P(z_i = k) = \pi_k \quad (3)$$

588

589 where X_i is a vector of $K - 1$ \log_2 SNR ratios, z_i indicates the identity of the target ($k =$
 590 $1, 2, \dots, K$), and $\Theta_k = \{M_k, \Sigma_k, \pi_k\}$ is the set of parameters of the Gaussian PDF \mathbb{N} and the prior
 591 probability that a detected target belonging to class k . The total joint likelihood for N detected
 592 targets is then

$$593 \quad L(\Theta; X) = P(X|\Theta) = \prod_{i=1}^N P(X_i|\Theta) = \prod_{i=1}^N \sum_{j=1}^K \pi_j \mathbb{N}(M_j, \Sigma_j) \quad (4)$$

594
 595 with $\Theta = \{\Theta_1, \Theta_2 \dots \Theta_K\}$ and $X = \{X_1, X_2 \dots X_N\}$. We use an expectation-maximization (EM)
 596 algorithm to iteratively calculate the maximum likelihood estimates of the model parameters
 597 where the E-step calculates the posterior probability via Bayes rule,

$$598 \quad P(z_i = k|X_i, \Theta) = \frac{\pi_k \mathbb{N}(M_k, \Sigma_k)}{\sum_{j=1}^K \pi_j \mathbb{N}(M_j, \Sigma_j)} \quad (5)$$

600
 601 and the M-step updates the model parameters for each class,

$$602 \quad \pi_k = \frac{\sum_{i=1}^N P(z_i = k|X_i, \Theta)}{N} \quad (6)$$

$$603 \quad M_k = \frac{\sum_{i=1}^N X_i \cdot P(z_i = k|X_i, \Theta)}{\sum_{i=1}^N P(z_i = k|X_i, \Theta)} \quad (7)$$

$$604 \quad \Sigma_k = \frac{\sum_{i=1}^N P(z_i = k|X_i, \Theta) (X_i - M_k)(X_i - M_k)^T}{\sum_{i=1}^N P(z_i = k|X_i, \Theta)} \quad (8)$$

605
 606
 607
 608
 609
 610 Prior probabilities (π) can be set by subjective assessment based on the experiment, or set to
 611 $1/K$ where all classes have equal probability. For example, to determine the relative probability
 612 that an LN 60S-detected nuclear target belongs to the LN 60S or EN 60S class, we assume that
 613 their relative frequencies are the same and therefore the prior probability of the two intermediates
 614 in the nucleus is equal: $P(LN\ 60S) = P(EN\ 60S) = 0.5$.

615
 616 **Data availability:**

617 Micrographs, templates and scaled maximum intensity projections (MIPs) in this study are
 618 accessible with the following public access code: EMPIAR-10998

619

620 **Acknowledgements:**

621 We are grateful to Michael Rosbash (Brandeis) for providing MNY8 cells, Xiaowei Zhao for
622 help trouble-shooting FIB-milling, and Peter Rickgauer, Tim Grant and Ben Himes for helpful
623 comments and suggestions. BL and NG acknowledge support from the Chan Zuckerberg
624 Initiative (VPI-0000000116).

625

626 **References:**

- 627 Delavoie F, Soldan V, Rinaldi D, Dauxois JY, Gleizes PE. 2019. The path of pre-ribosomes
628 through the nuclear pore complex revealed by electron tomography. *Nature*
629 *Communications* **10**:1–12. doi:10.1038/s41467-019-08342-7
- 630 Erdmann PS, Hou Z, Klumpe S, Khavnekar S, Beck F, Wilfling F, Plitzko JM, Baumeister W.
631 2021. In situ cryo-electron tomography reveals gradient organization of ribosome
632 biogenesis in intact nucleoli. *Nature Communications* **12**:1–9. doi:10.1038/s41467-021-
633 25413-w
- 634 Grant T, Rohou A, Grigorieff N. 2018. CisTEM, user-friendly software for single-particle image
635 processing. *Elife* **7**:e35383. doi:10.7554/eLife.35383
- 636 Gubins I, Chaillet ML, van der Schot G, Veltkamp RC, Förster F, Hao Y, Wan X, Cui X, Zhang
637 F, Moebel E, Wang X, Kihara D, Zeng X, Xu M, Nguyen NP, White T, Bunyak F. 2020.
638 SHREC 2020: Classification in cryo-electron tomograms. *Computers & Graphics* **91**:279–
639 289. doi:10.1016/J.CAG.2020.07.010
- 640 Himes B, Grigorieff N. 2021. Cryo-TEM simulations of amorphous radiation-sensitive samples
641 using multislice wave propagation. *urn:issn:2052-2525* **8**:943–953.
642 doi:10.1107/S2052252521008538
- 643 Himes BA, Zhang P. 2018. emClarity: software for high-resolution cryo-electron tomography
644 and subtomogram averaging. *Nature Methods* **15**:955–961. doi:10.1038/s41592-018-0167-z
- 645 Ho JHN, Kallstrom G, Johnson AW. 2000. Nmd3p Is a Crm1p-Dependent Adapter Protein for
646 Nuclear Export of the Large Ribosomal Subunit. *The Journal of Cell Biology* **151**:1057.
647 doi:10.1083/JCB.151.5.1057
- 648 Jumper J, Evans R, Pritzel A, Green T, Figurnov M, Ronneberger O, Tunyasuvunakool K, Bates
649 R, Židek A, Potapenko A, Bridgland A, Meyer C, Kohl SAA, Ballard AJ, Cowie A,
650 Romera-Paredes B, Nikolov S, Jain R, Adler J, Back T, Petersen S, Reiman D, Clancy E,
651 Zielinski M, Steinegger M, Pacholska M, Berghammer T, Bodenstein S, Silver D, Vinyals
652 O, Senior AW, Kavukcuoglu K, Kohli P, Hassabis D. 2021. Highly accurate protein
653 structure prediction with AlphaFold. *Nature* **596**:583–589. doi:10.1038/s41586-021-03819-
654 2
- 655 Kürner J, Frangakis AS, Baumeister W. 2005. Cryo-electron tomography reveals the cytoskeletal
656 structure of *Spiroplasma melliferum*. *Science* **307**:436–438. doi:10.1126/science.1104031
- 657 Leidig C, Thoms M, Holdermann I, Bradatsch B, Berninghausen O, Bange G, Sinning I, Hurt E,
658 Beckmann R. 2014. 60S ribosome biogenesis requires rotation of the 5S ribonucleoprotein
659 particle. *Nature Communications* **5**:3491. doi:10.1038/ncomms4491

- 660 Lucas BA, Himes BA, Xue L, Grant T, Mahamid J, Grigorieff N. 2021. Locating
661 macromolecular assemblies in cells by 2D template matching with cisTEM. *Elife* **10**.
662 doi:10.7554/elife.68946
- 663 Lučić V, Rigort A, Baumeister W. 2013. Cryo-electron tomography: The challenge of doing
664 structural biology in situ. *Journal of Cell Biology* **202**:407–419.
665 doi:10.1083/JCB.201304193
- 666 Mahamid J, Pfeffer S, Schaffer M, Villa E, Danev R, Cuellar LK, Förster F, Hyman AA, Plitzko
667 JM, Baumeister W. 2016. Visualizing the molecular sociology at the HeLa cell nuclear
668 periphery. *Science* **351**:969–972. doi:10.1126/science.aad8857
- 669 Marko M, Hsieh C, Schalek R, Frank J, Mannella C. 2007. Focused-ion-beam thinning of
670 frozen-hydrated biological specimens for cryo-electron microscopy. *Nature Methods* **4**:215–
671 217. doi:10.1038/nmeth1014
- 672 Matsuo Y, Granneman S, Thoms M, Manikas RG, Tollervey D, Hurt E. 2014. Coupled GTPase
673 and remodelling ATPase activities form a checkpoint for ribosome export. *Nature* **505**:112–
674 116. doi:10.1038/nature12731
- 675 Meng EC, Pettersen EF, Couch GS, Huang CC, Ferrin TE. 2006. Tools for integrated sequence-
676 structure analysis with UCSF Chimera. *BMC Bioinformatics* **7**:339. doi:10.1186/1471-
677 2105-7-339
- 678 Moebel E, Martinez-Sanchez A, Lamm L, Righetto RD, Wietrzynski W, Albert S, Larivière D,
679 Fourmentin E, Pfeffer S, Ortiz J, Baumeister W, Peng T, Engel BD, Kervrann C. 2021.
680 Deep learning improves macromolecule identification in 3D cellular cryo-electron
681 tomograms. *Nature Methods* 1–9. doi:10.1038/s41592-021-01275-4
- 682 Pedregosa F, Varoquaux G, Gramfort A, Michel V, Thirion B, Grisel O, Blondel M, Prettenhofer
683 P, Weiss R, Dubourg V, Vanderplas J, Passos A, Cournapeau D, Brucher M, Perrot M,
684 Duchesnay E. 2011. Scikit-learn: Machine Learning in Python. *Journal of Machine
685 Learning Research* **12**:2825–2830.
- 686 Pertschy B, Saveanu C, Zisser G, Lebreton A, Tengg M, Jacquier A, Liebminger E, Nobis B,
687 Kappel L, van der Klei I, Högenauer G, Fromont-Racine M, Bergler H. 2007. Cytoplasmic
688 Recycling of 60S Preribosomal Factors Depends on the AAA Protein Drg1. *Molecular and
689 Cellular Biology* **27**:6581–6592. doi:10.1128/mcb.00668-07
- 690 Pettersen EF, Goddard TD, Huang CC, Couch GS, Greenblatt DM, Meng EC, Ferrin TE. 2004.
691 UCSF Chimera—A visualization system for exploratory research and analysis. *Journal of
692 Computational Chemistry* **25**:1605–1612. doi:10.1002/JCC.20084
- 693 Pettersen EF, Goddard TD, Huang CC, Meng EC, Couch GS, Croll TI, Morris JH, Ferrin TE.
694 2021. UCSF ChimeraX: Structure visualization for researchers, educators, and developers.
695 *Protein Science : A Publication of the Protein Society* **30**:70. doi:10.1002/PRO.3943
- 696 Rickgauer JP, Choi H, Lippincott-Schwartz J, Denk W. 2020. Label-free single-instance protein
697 detection in vitrified cells. *bioRxiv* 2020.04.22.053868. doi:10.1101/2020.04.22.053868
- 698 Rickgauer JP, Grigorieff N, Denk W. 2017. Single-protein detection in crowded molecular
699 environments in cryo-EM images. *Elife* **6**:e25648. doi:10.7554/elife.25648
- 700 Rigort A, Bäuerlein FJB, Villa E, Eibauer M, Laugks T, Baumeister W, Plitzko JM. 2012.
701 Focused ion beam micromachining of eukaryotic cells for cryoelectron tomography. *Proc
702 Natl Acad Sci U S A* **109**:4449–4454. doi:10.1073/pnas.1201333109
- 703 Rohou A, Grigorieff N. 2015. CTFFIND4: Fast and accurate defocus estimation from electron
704 micrographs. *Journal of Structural Biology* **192**:216–221. doi:10.1016/J.JSB.2015.08.008

- 705 Rosenthal PB, Henderson R. 2003. Optimal Determination of Particle Orientation, Absolute
706 Hand, and Contrast Loss in Single-particle Electron Cryomicroscopy. *Journal of Molecular*
707 *Biology* **333**:721–745. doi:10.1016/J.JMB.2003.07.013
- 708 Schaffer M, Pfeffer S, Mahamid J, Kleindiek S, Laugks T, Albert S, Engel BD, Rummel A,
709 Smith AJ, Baumeister W, Plitzko JM. 2019. A cryo-FIB lift-out technique enables
710 molecular-resolution cryo-ET within native *Caenorhabditis elegans* tissue. *Nature Methods*
711 **16**:757–762. doi:10.1038/s41592-019-0497-5
- 712 Schur FKM, Obr M, Hagen WJH, Wan W, Jakobi AJ, Kirkpatrick JM, Sachse C, Kräusslich HG,
713 Briggs JAG. 2016. An atomic model of HIV-1 capsid-SP1 reveals structures regulating
714 assembly and maturation. *Science* **353**:506–508. doi:10.1126/science.aaf9620
- 715 Tegunov D, Xue L, Dienemann C, Cramer P, Mahamid J. 2021. Multi-particle cryo-EM
716 refinement with M visualizes ribosome-antibiotic complex at 3.5 Å in cells. *Nature Methods*
717 **18**:186–193. doi:10.1038/s41592-020-01054-7
- 718 Tesina P, Heckel E, Cheng J, Fromont-Racine M, Buschauer R, Kater L, Beatrix B,
719 Berninghausen O, Jacquier A, Becker T, Beckmann R. 2019. Structure of the 80S
720 ribosome–Xrn1 nuclease complex. *Nature Structural & Molecular Biology* **26**:275–280.
721 doi:10.1038/s41594-019-0202-5
- 722 Vilas JL, Oton J, Messaoudi C, Melero R, Conesa P, Ramirez-Aportela E, Mota J, Martinez M,
723 Jimenez A, Marabini R, Carazo JM, Vargas J, Sorzano COS. 2020. Measurement of local
724 resolution in electron tomography. *Journal of Structural Biology* **4**:100016.
725 doi:10.1016/J.YJSBX.2019.100016
- 726 Villa E, Schaffer M, Plitzko JM, Baumeister W. 2013. Opening windows into the cell: focused-
727 ion-beam milling for cryo-electron tomography. *Current Opinion in Structural Biology*
728 **23**:771–777. doi:10.1016/J.SBI.2013.08.006
- 729 von der Haar T. 2008. A quantitative estimation of the global translational activity in
730 logarithmically growing yeast cells. *BMC Systems Biology* **2**:87. doi:10.1186/1752-0509-2-
731 87
- 732 Warner JR. 1999. The economics of ribosome biosynthesis in yeast. *Trends Biochem Sci* **24**:437–
733 440. doi:10.1016/S0968-0004(99)01460-7
- 734 Wu S, Tutuncuoglu B, Yan K, Brown H, Zhang Y, Tan D, Gamalinda M, Yuan Y, Li Z,
735 Jakovljevic J, Ma C, Lei J, Dong MQ, Woolford JL, Gao N. 2016. Diverse roles of
736 assembly factors revealed by structures of late nuclear pre-60S ribosomes. *Nature* **534**:133–
737 137. doi:10.1038/nature17942
- 738 Xue L, Lenz S, Zimmermann-Kogadeeva M, Tegunov D, Cramer P, Bork P, Rappsilber J,
739 Mahamid J. 2021. Visualizing translation dynamics at atomic detail inside a bacterial cell.
740 *bioRxiv* 2021.12.18.473270. doi:10.1101/2021.12.18.473270
- 741 Zhou Y, Musalgaonkar S, Johnson AW, Taylor DW. 2019. Tightly-orchestrated rearrangements
742 govern catalytic center assembly of the ribosome. *Nature Communications* **10**.
743 doi:10.1038/s41467-019-08880-0
- 744
- 745

746 **Figure Legends:**

747

748 **Figure 1: Detection of cytoplasmic mature 60S and mitochondrial ribosomes in 2D images**

749 **of FIB-milled yeast lamella.** A) Cryo-EM like density generated using the atomic coordinates of
750 PDB:6Q8Y that correspond with the mature 60S. B) TEM image of the nuclear periphery from a
751 FIB-milled yeast lamella. Yellow arrows indicate low-resolution features in the cytoplasm that
752 may indicate the presence of ribosomes. Blue arrows indicate regions of similar size and contrast
753 in the nucleoplasm. NE: nuclear envelope; NPC: nuclear pore complex. C) Cryo-EM micrograph
754 of yeast nuclear periphery from FIB-milled lamella with the results from a 2DTM search using
755 the mature 60S template. Significant targets are indicated by mapping the template in the best
756 matching locations and orientations (shown in yellow). The red box indicates the regions
757 highlighted in E) and F). Scale bar = 50 nm. D) Bar chart indicating the number of mature 60S-
758 detected targets identified in the indicated subcellular compartments in 28 images of the nuclear
759 periphery. E) Scaled maximum intensity projection (MIP) showing the results of 2DTM using
760 the template in A) in the region of C) indicated in red. F) 3D slab indicating the locations and
761 orientations of mature 60S-detected targets in the indicated region of C). The red polypeptide
762 indicates the location of the polypeptide exit tunnel on each 60S. G) Plot showing the density of
763 mature 60S in the regions of the images corresponding to the cytoplasm. Each dot represents a
764 different image. The solid black bar indicates the median. H) 10 Å filtered 3D reconstruction
765 calculated from 3991 60S subunits at the locations and orientations detected in 28 images,
766 showing clear density for the 40S small subunit. The molecular model of the 60S used to
767 generate the template in A) is shown in yellow.

768

769 **Figure 2: 2DTM SNRs differentiate cytoplasmic mature 60S from nuclear pre-60S in 2D**

770 **images of FIB-milled yeast lamella.** A) Diagram showing the compositional changes that
771 accompany the maturation from the late nuclear (LN) 60S (PDB: 6N8J), shown in blue, to the
772 mature 60S (PDB: 6Q8Y), shown in yellow, in the cytoplasm. B) Cryo-EM micrograph of yeast
773 nuclear periphery from FIB-milled lamella with the results from a 2DTM search using the LN
774 60S template. Significant targets are indicated by mapping a projection of the template in the
775 best matching locations and orientations (shown in blue). Scale bar = 50 nm. C) As in B),
776 showing the results from a 2DTM search of the indicated image using the mature 60S as a

777 template (yellow). D) Maximum intensity projection showing the results of a 2DTM search with
778 the LN 60S template in the region of the image in B) highlighted in orange. Orange circles
779 indicate two targets identified by both LN 60S and mature 60S. E) As in D) showing the results
780 of a 2DTM search with the mature 60S template in the region of the image in C) highlighted in
781 orange. F) As in D) corresponding to the region of B) highlighted in blue and circles indicating
782 two LN 60S-detected targets. G) As in D) showing the results of a 2DTM search with the mature
783 60S template in the region of the image in C) highlighted in blue. H) Diagram indicating the
784 number of mature 60S (yellow) and LN 60S (blue)-detected targets identified in 2DTM searches
785 of 28 images of the nuclear periphery. The overlap of the Venn diagram indicates the number of
786 targets identified in both searches. I) Bar chart indicating the number of targets detected by the
787 mature 60S (yellow), the LN 60S (blue), and by both (black) in regions of the images
788 corresponding to the nucleus or cytoplasm. J) Plot showing the \log_2 2DTM SNR ratios for LN
789 and mature 60S-detected targets grouped by subcellular compartment. Each dot indicates a 60S
790 detected in both searches. ****: $p < 0.0001$. K) Image showing the identified targets color-coded
791 by the best-matching template (blue: LN 60S, yellow: mature 60S) as determined by the higher
792 2DTM SNR at each overlapping location. Scale bar = 50 nm. L) Pie chart indicating the
793 proportion of all nuclear (left) and cytoplasmic (right) 60S targets that more closely resemble the
794 mature 60S (yellow) or LN 60S (blue) template, respectively, as determined by the highest
795 2DTM SNR at each identified location and orientation.

796

797 **Figure 3: Relative probability of detecting mature or LN 60S.** A) Histogram showing the
798 distribution of the mature 60S / LN 60S 2DTM SNR ratios for each LN and mature 60S-detected
799 target fit with two Gaussians indicating populations 1 (blue dashed line) and 2 (red dashed line).
800 The black line indicates the sum of the two Gaussians, $R^2 = 0.993$. B) Line graph showing the
801 probability that a given target belongs to the LN 60S population (blue) line, or mature 60S
802 population (red), as a function of \log_2 2DTM SNR ratio. C) Line graph showing the fraction of
803 nuclear (blue) and cytoplasmic (red) targets classified as LN 60S, at the indicated confidence
804 intervals determined using Eq (5). D) Heat map showing the probability of each LN and mature
805 60S-detected target belonging to either the LN or mature 60S populations. Each row indicates a
806 detected target, and the rows are sorted by their subcellular distribution. The targets assigned to

807 the mature 60S population are indicated in yellow and the targets assigned to the LN 60S
808 population are indicated in blue.

809

810 **Figure 4: Classification of cytoplasmic mature 60S and nuclear pre-60S by 2DTM**

811 **corresponds with biologically relevant differences in the templates.** A) The LN 60S (blue)
812 and mature 60S (yellow) 2DTM templates aligned in UCSF Chimera. B) LN 60S with difference
813 map calculated using UCSF Chimera showing the density in the LN 60S template that is not
814 present in the mature 60S template (red, transparent). C) As in B), showing the mature 60S with
815 density that is not in common with the LN 60S template (red, transparent). D) Boxplots showing
816 the change in 2DTM SNR when only RNA (left) or protein (right) components of the LN 60S
817 template are included, relative to the full-length template for each significant target. The targets
818 are grouped by their subcellular localization. E) Upper: LN 60S template with all ribosome
819 biogenesis factors (RBFs) indicated in red. Lower: Boxplot showing the change in the 2DTM
820 SNR of the nuclear (blue) and cytoplasmic (red) targets when all RBFs are removed, relative to
821 the full-length LN 60S template in untreated cells, and when Crm1-mediated nuclear export is
822 inhibited by treating Crm1(T539C) cells with Leptomycin B (LepB). Box width indicates the
823 interquartile range, the central line indicates the median and the whiskers indicate the range of
824 95% of the targets. F) As in E), for RBF Nog1. G) As in E), for RBF Nog2. ****: $p < 0.0001$, ns:
825 not significant ($p > 0.05$).

826

827 **Figure 5: Classification of nuclear targets by relative similarity to early or late nuclear**

828 **intermediates.** A) Venn diagram showing the number of significant targets detected in 2DTM
829 searches with the indicated templates. Overlap indicates targets identified in two or more
830 searches. B) Venn diagrams showing the number of significant targets detected in 2DTM
831 searches with the indicated templates in the nucleus (left) and cytoplasm (right). C) Scatterplot
832 showing the EN 60S / LN 60S 2DTM SNR ratios relative to the mature 60S / LN 60S 2DTM
833 SNR ratios for each EN, LN and mature 60S-detected target. Ellipses indicate the fits of three
834 Gaussians and each concentric ellipse indicates one standard deviation from the mean. Each
835 target is colored according to its most likely class membership. D) Heat map showing the
836 probability of each of the targets examined in C) belonging to one of the populations, EN, LN or
837 mature 60S. Targets are grouped by their subcellular localization, followed by their classification

838 as EN 60S (purple), LN 60S (light blue), or mature 60S (yellow). E) Bar chart showing the
839 proportion of the LN 60S-detected targets in the indicated cells that are classified as LN 60S
840 (blue), mature 60S (yellow) or EN 60S (purple). F) Cryo-EM micrograph of the yeast nuclear
841 periphery from a FIB-milled lamella shown in in **Figure 1**, displaying the results of 2DTM
842 searches, colored by their classification as mature 60S (yellow), LN 60S (blue) or EN 60S
843 (purple) based on their relative 2DTM SNRs.

844

845 **Figure 1 — figure supplement 1:** A) FIB-image of two yeast cells frozen on a cryo-EM grid. B)
846 FIB image of the lamella after milling the cells shown in A). C) Survival histogram showing the
847 number of search locations with 2DTM SNR values above a given threshold from a 2DTM
848 search using the mature 60S template in **Figure 1A**. D) FSC obtained for the 3D reconstruction
849 shown in **Figure 1H** calculated using the targets identified by 2DTM.

850

851 **Figure 2 — figure supplement 1:** A) Venn diagrams showing the number of mature (yellow)
852 and LN 60S (blue) detected targets in the indicated subcellular compartments. The overlap
853 indicates targets detected in searches with both templates. B) Violin plot showing the kernelled
854 distribution of 2DTM SNRs of mature 60S-detected targets (left) and LN 60S-detected targets
855 (right) in the indicated subcellular compartments. ****: $p < 0.0001$, ns: not significant, $p > 0.05$. C)
856 Histogram showing the relative frequency of mature 60S / LN 60S 2DTM SNR ratios grouped
857 by subcellular localization. Gaussian fits are indicated by a solid line. D) Boxplot showing the
858 mature 60S / LN 60S 2DTM SNR ratios of the nuclear (blue) and cytoplasmic (red) populations
859 from each of the 28 images analyzed, indicating that the nuclear and cytoplasmic populations are
860 distinct, even within single images.

861

862 **Figure 3 — figure supplement 1:** A) Scatterplot showing the 2DTM SNRs for nuclear (blue)
863 and cytoplasmic (red) targets detected in searches with the LN and mature 60S templates. B)
864 Scatterplot showing P(LN 60S) for nuclear (blue) or cytoplasmic (red) LN 60S-detected target as
865 a function of the 2DTM SNR. Dotted line indicates the 2DTM threshold.

866

867 **Figure 4 — figure supplement 1:** A) TEM image of the nuclear periphery and vacuole in Crm1
868 (T539C) cells treated with Leptomycin B, overlaid with LN 60S-detected targets in blue. Scale
869 bar: 50 nm. B) Bar chart showing the number of LN and mature 60S-detected targets in the
870 indicated subcellular compartments. C) Violin plot showing the kernelled distribution of 2DTM
871 SNRs for LN 60S-detected targets in the indicated subcellular compartment. ****: $p < 0.0001$. D)
872 As in C), showing mature 60S-detected targets. ns: not significant, $p > 0.05$. E) Violin plot
873 showing the kernelled distribution of 2DTM SNR ratios of targets identified as both LN and
874 mature 60S-detected targets in the indicated subcellular compartment. ****: $p < 0.0001$.

875

876 **Figure 5 — figure supplement 1:** A) Violin plots showing the kernelled distribution of 2DTM
877 SNRs for EN 60S-detected targets in the indicated subcellular compartment. ****: $p < 0.0001$. B)
878 Histogram showing the distribution of EN 60S / LN 60S SNR ratios of EN and LN 60S-detected
879 targets in untreated cells. Targets are grouped by their subcellular distribution. Gaussian fits are
880 indicated in solid colors. C) TEM image of the nuclear periphery shown in **Figure 1**, overlaid

881 with EN 60S detected targets in purple. D) TEM image of the nuclear periphery. Scale bar
882 indicates 50 nm. E) The image in D) is shown overlaid with EN 60S-detected targets in purple,
883 F) LN 60S-detected targets in blue or G) mature 60S-detected targets in yellow. H) As in E)
884 showing the results of 2DTM searches, colored by their classification as mature 60S (yellow),
885 LN 60S (blue) or EN 60S (purple) based on their relative 2DTM SNRs
886
887

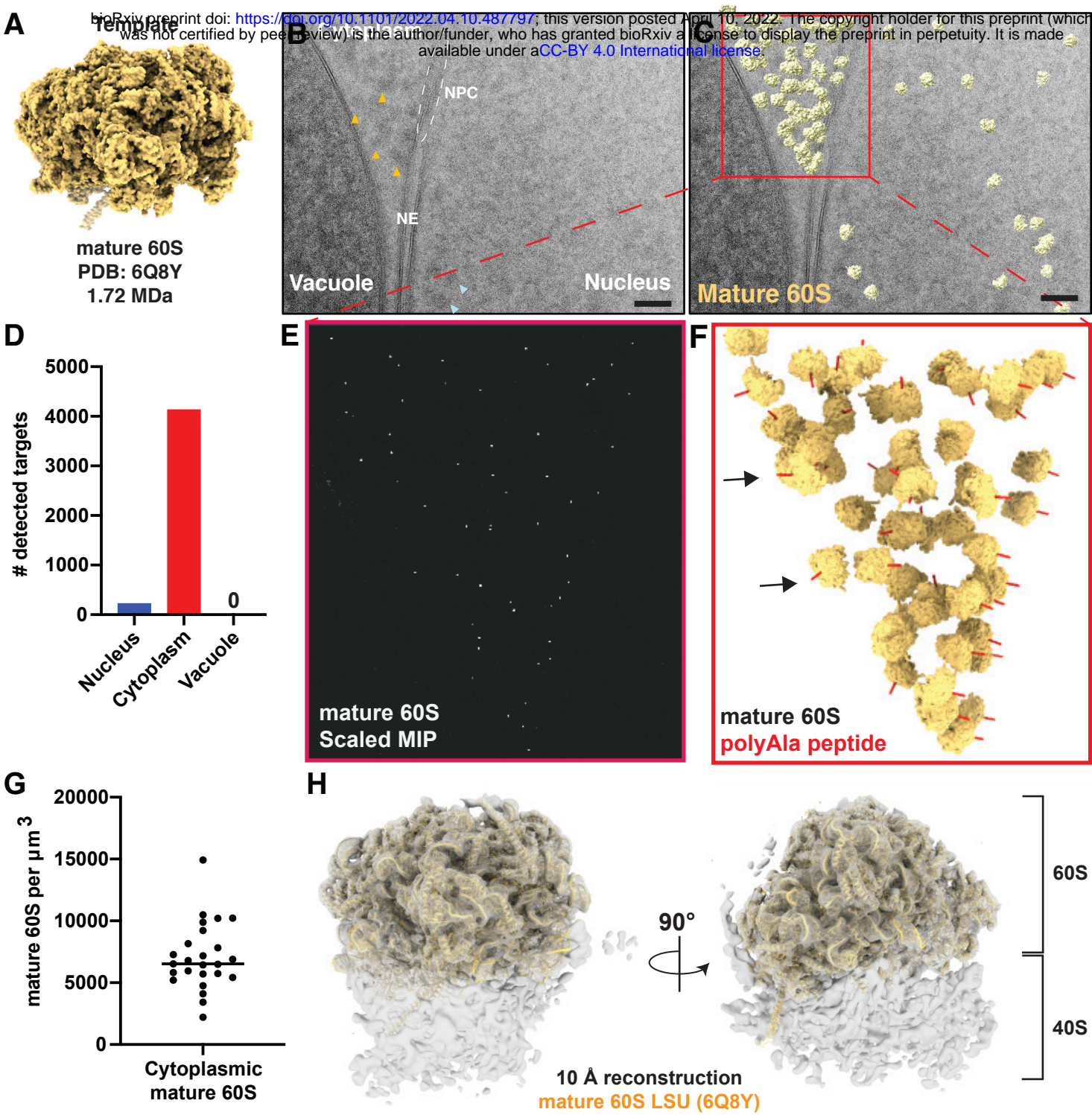


Figure 1

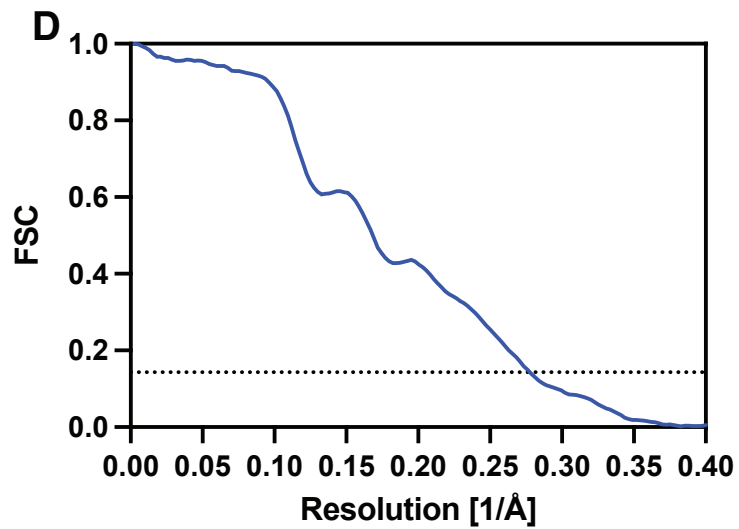
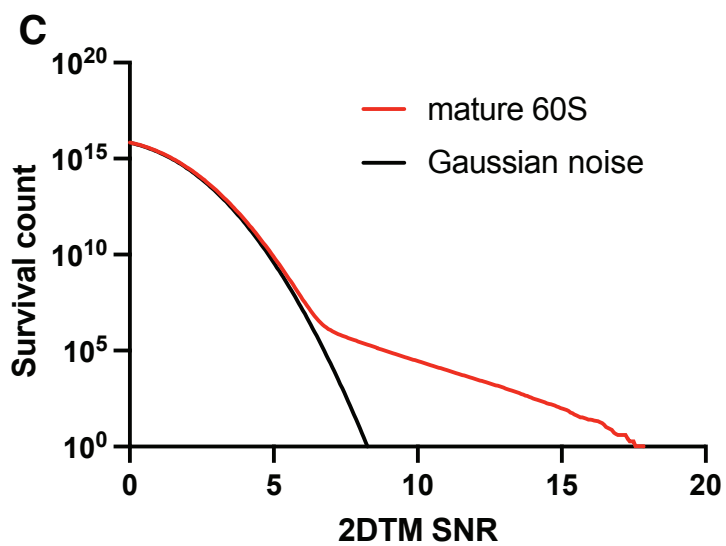
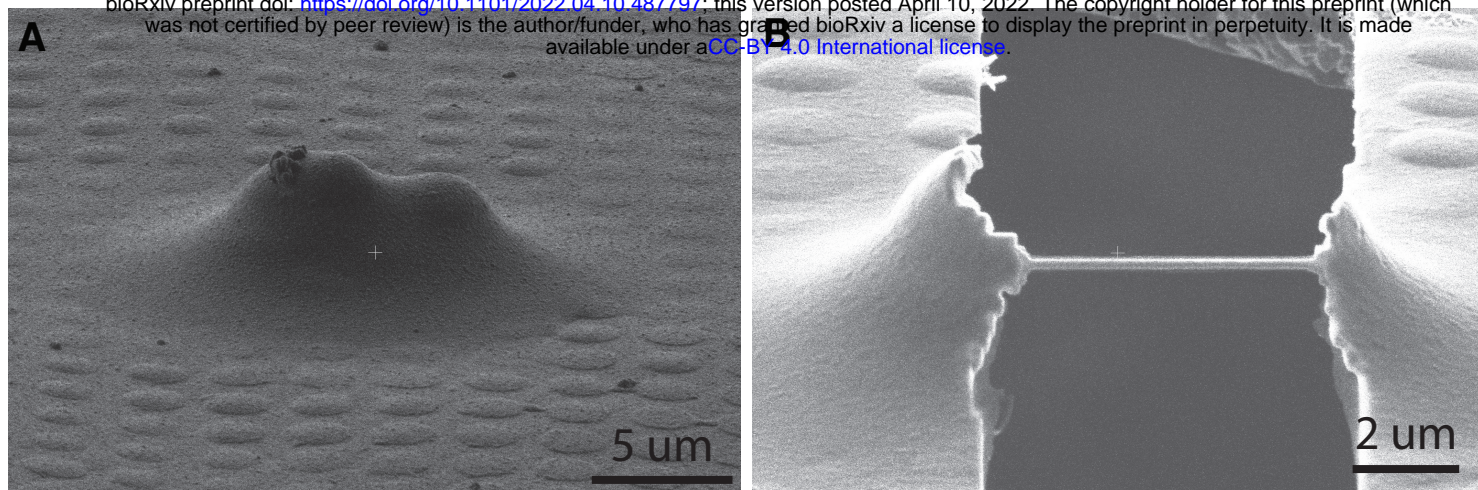


Figure 1 - figure supplement 1

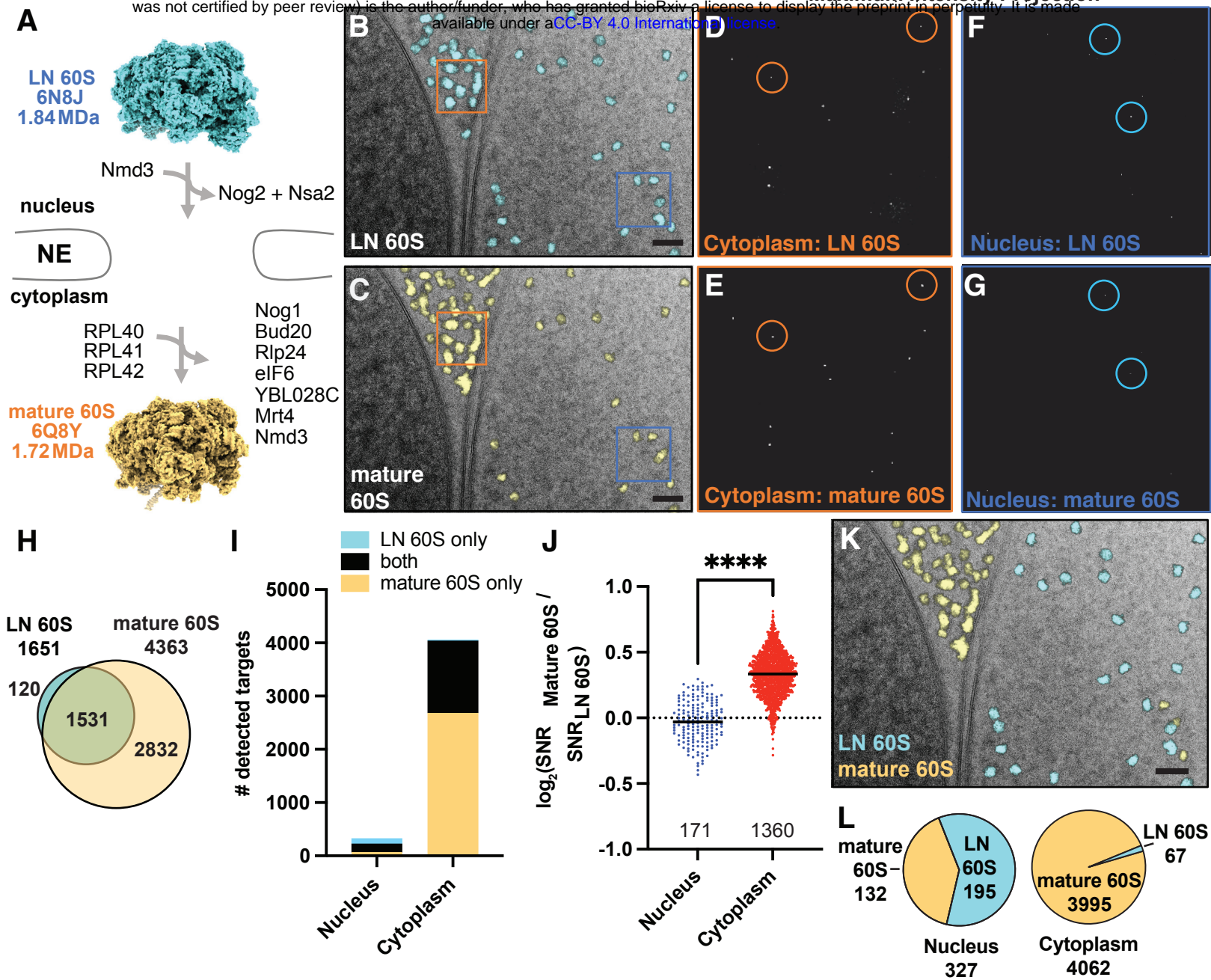


Figure 2

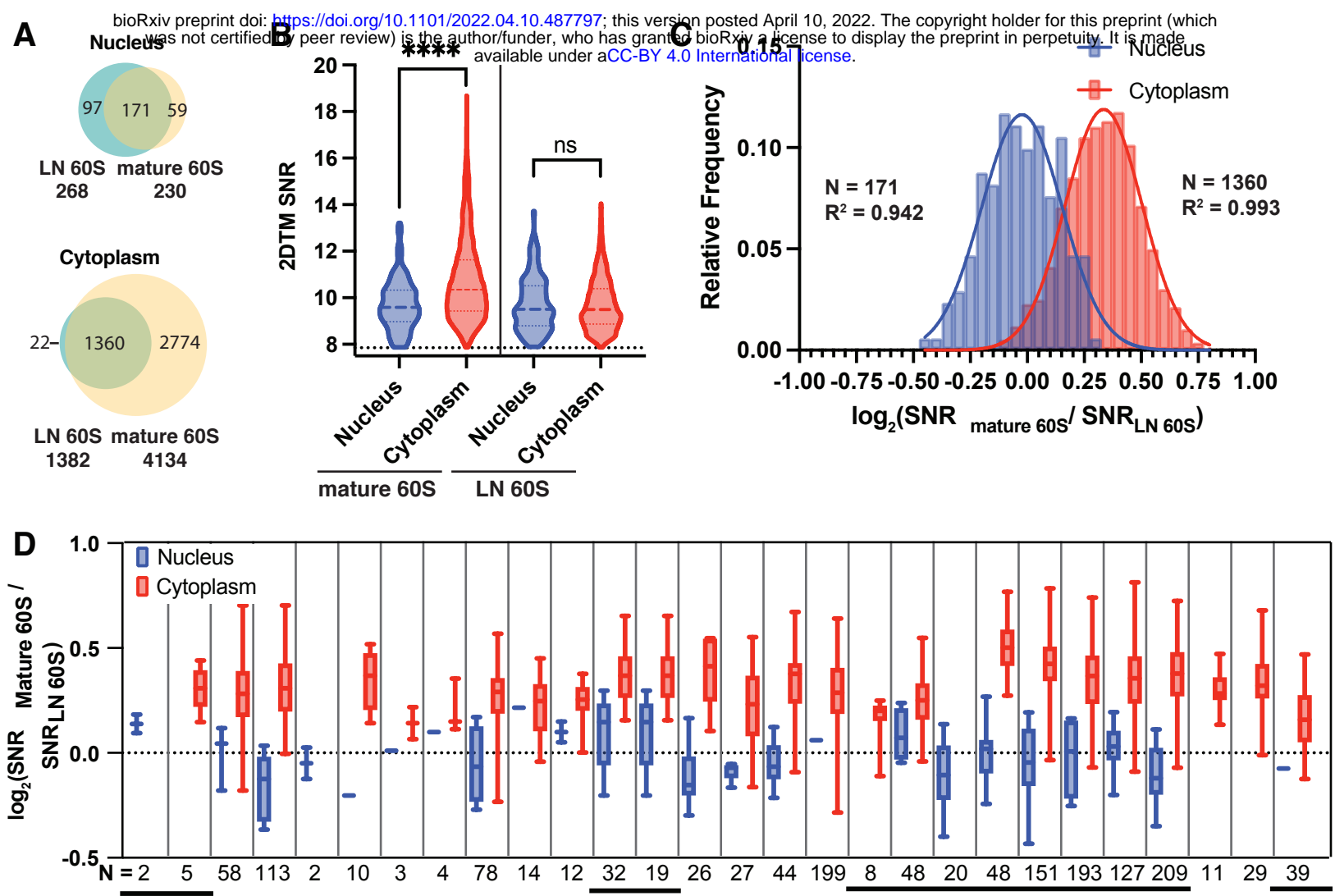


Figure 2 - figure supplement 1

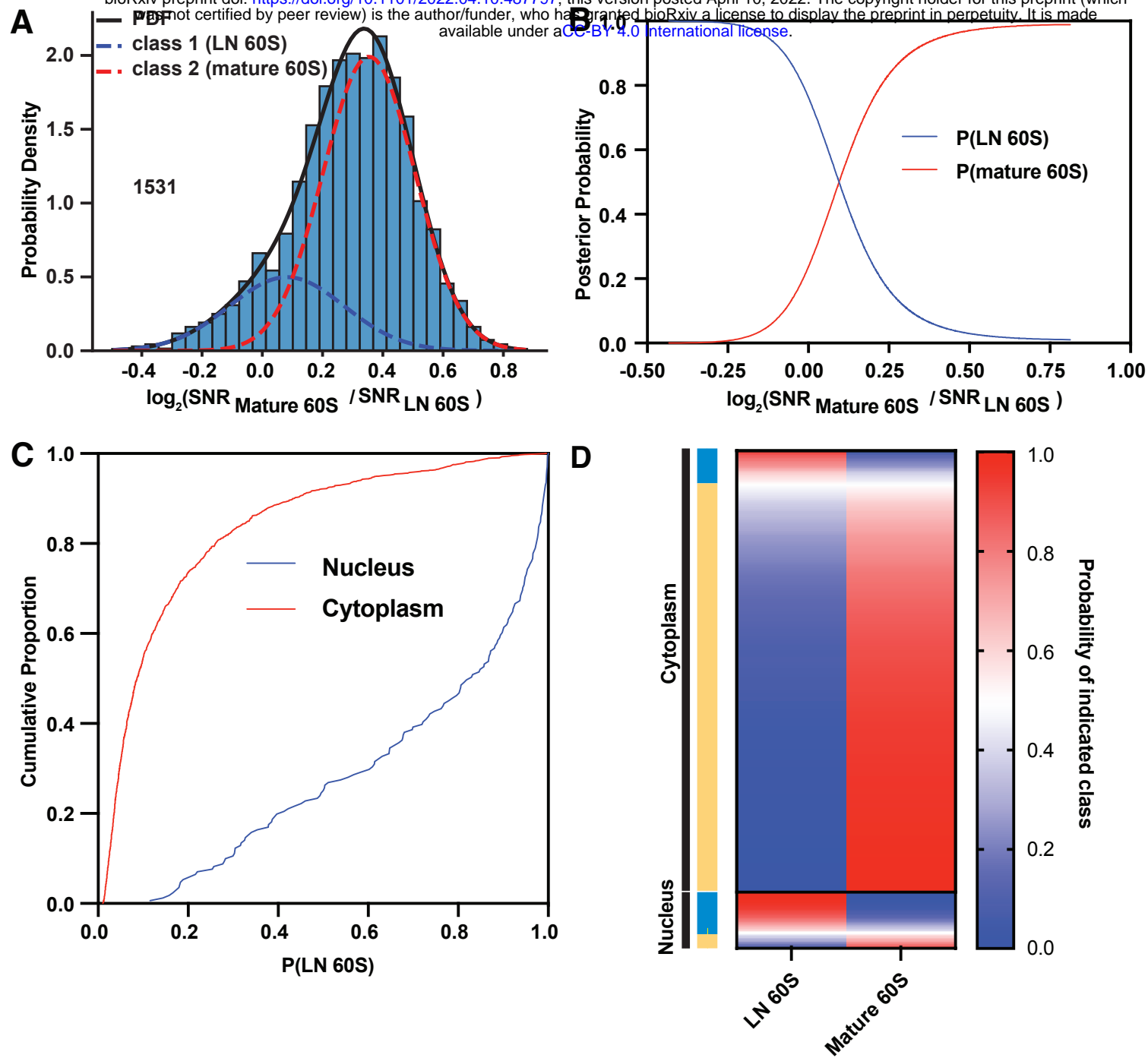
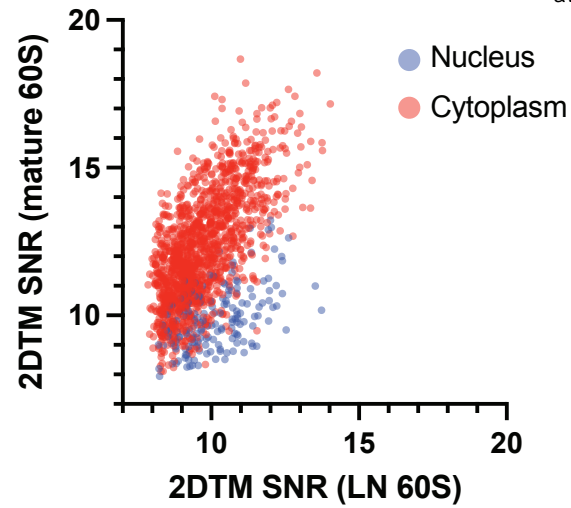


Figure 3

A



B

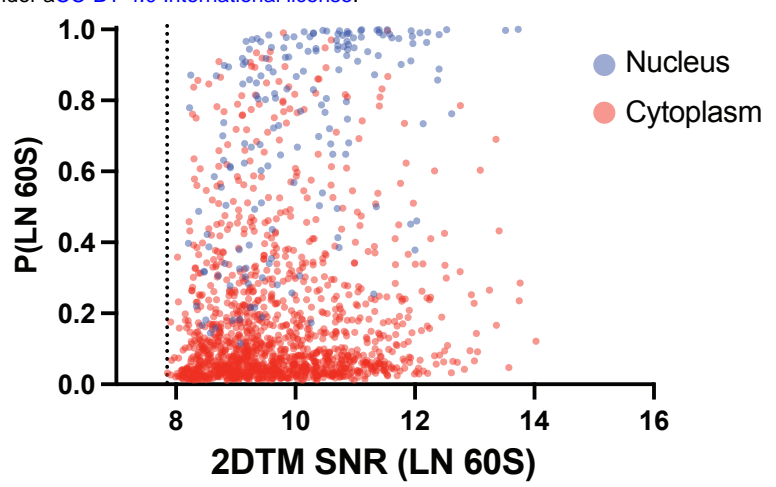


Figure 3 - figure supplement 1

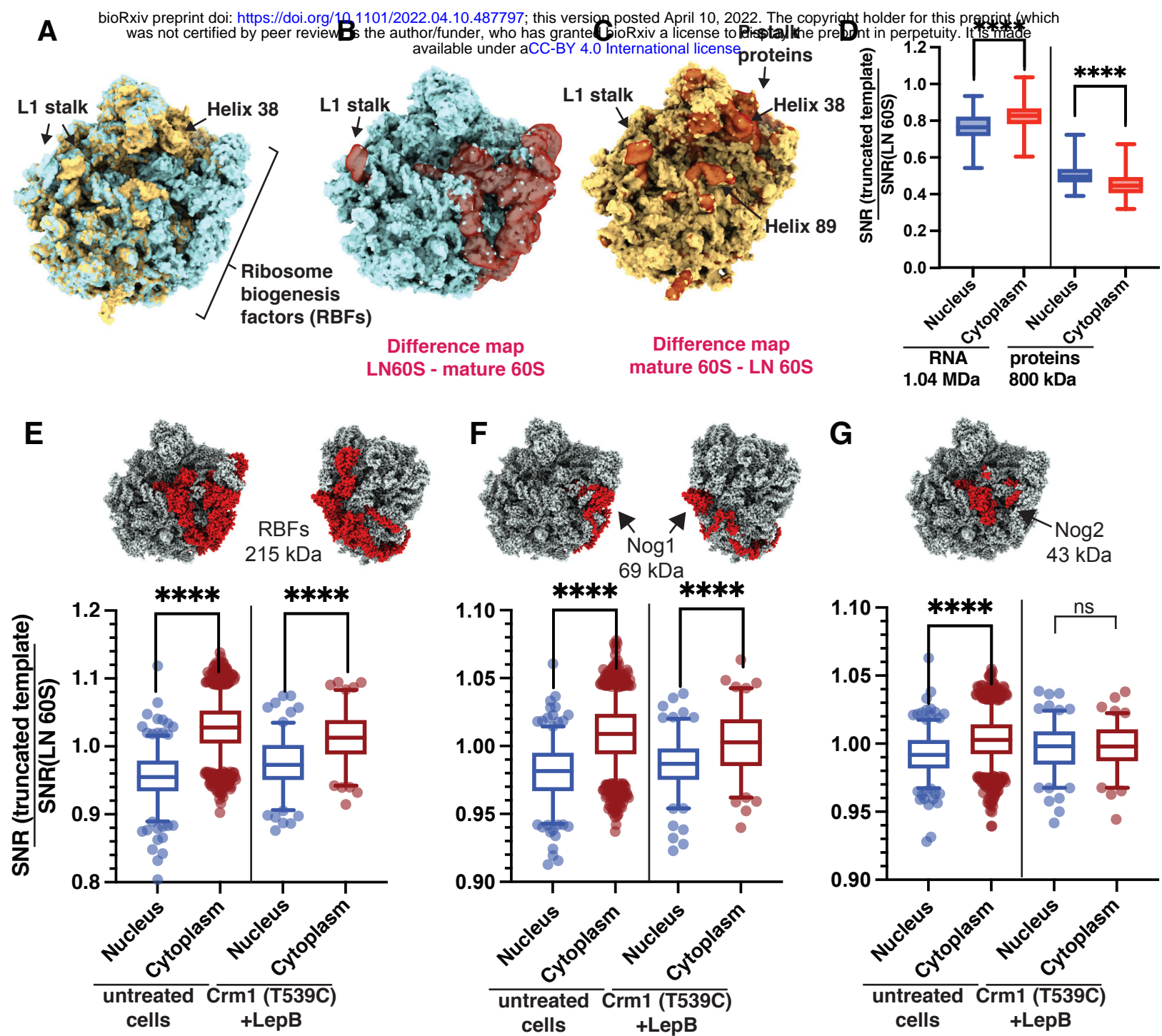


Figure 4

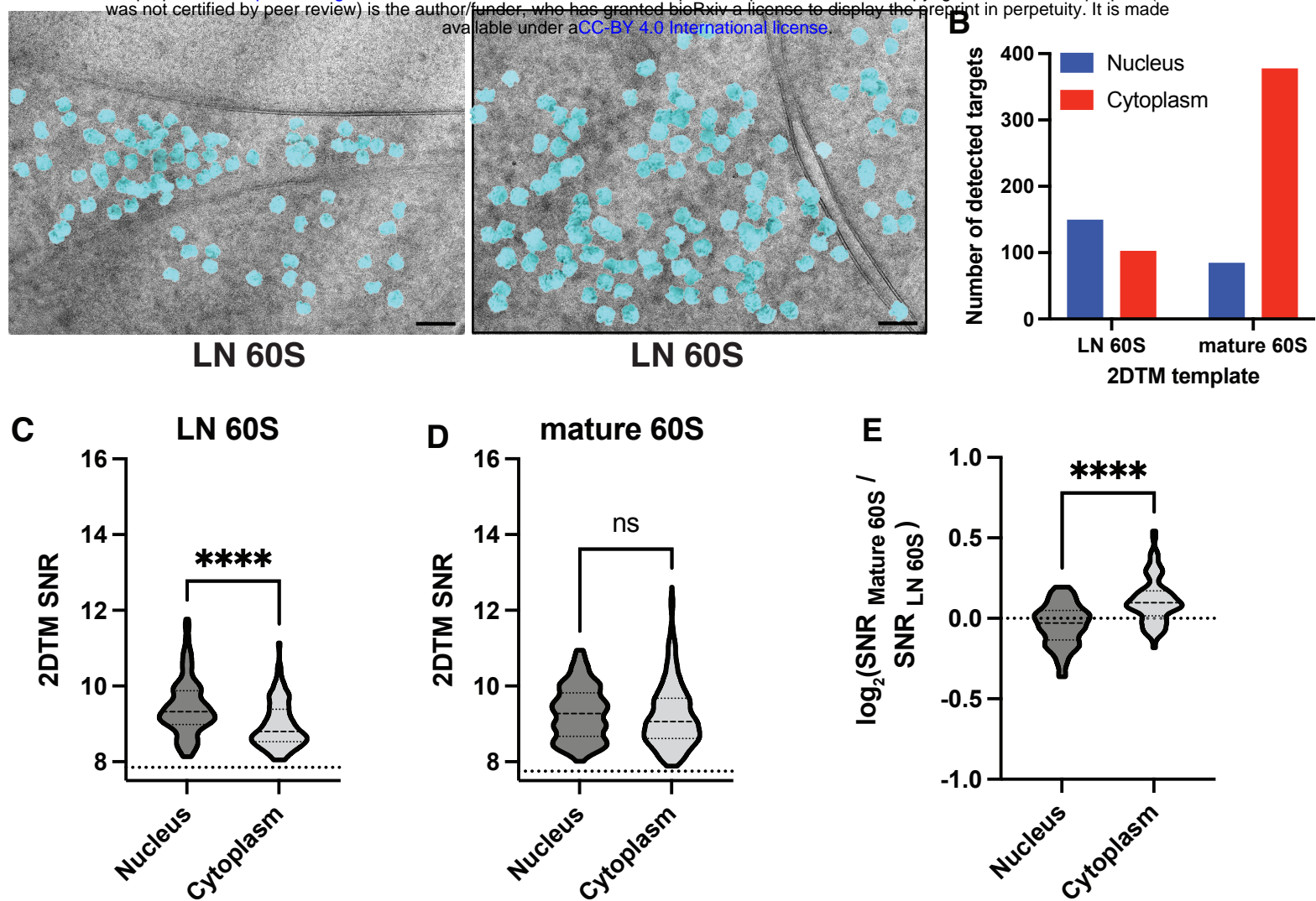


Figure 4 - figure supplement 1

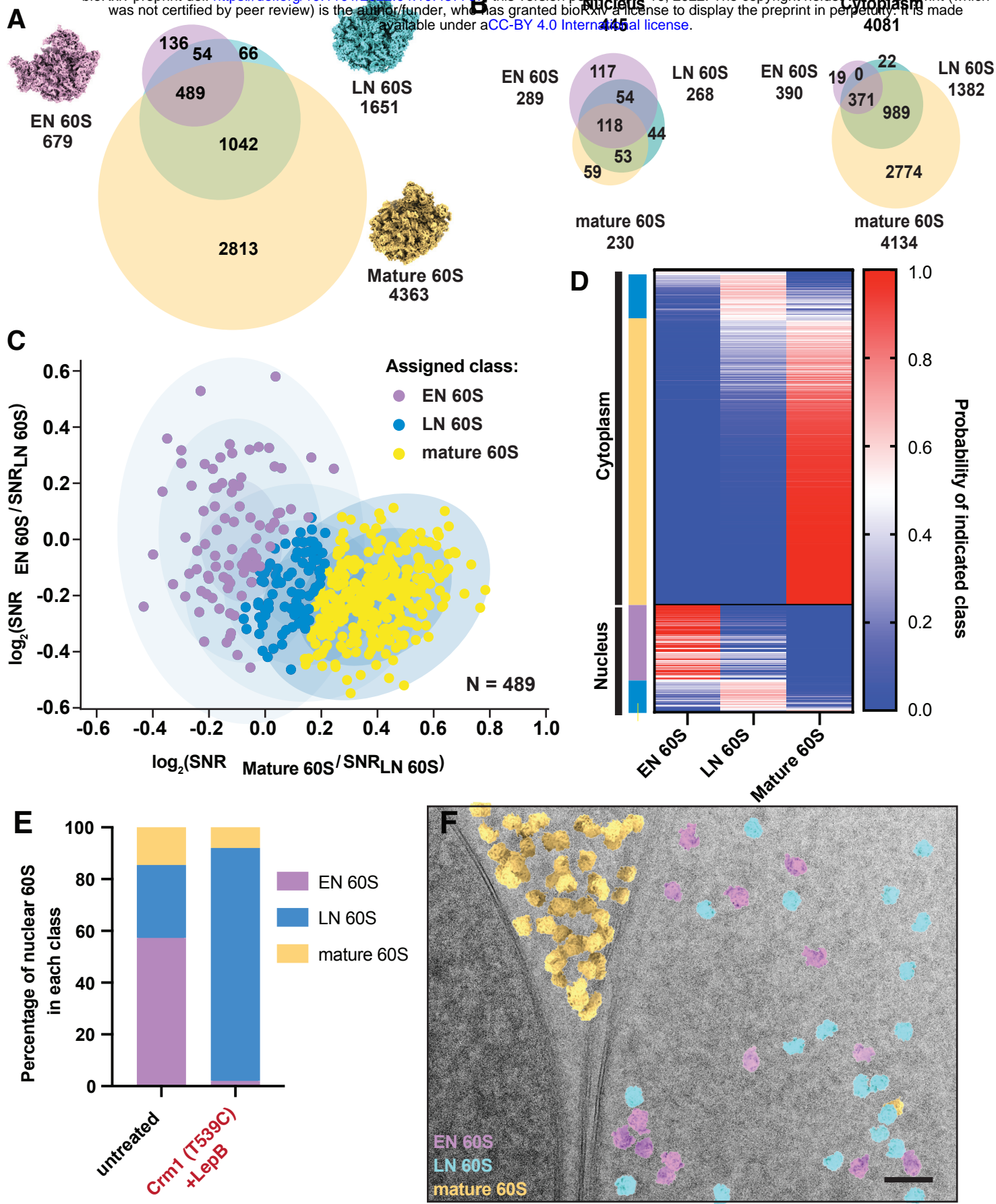


Figure 5

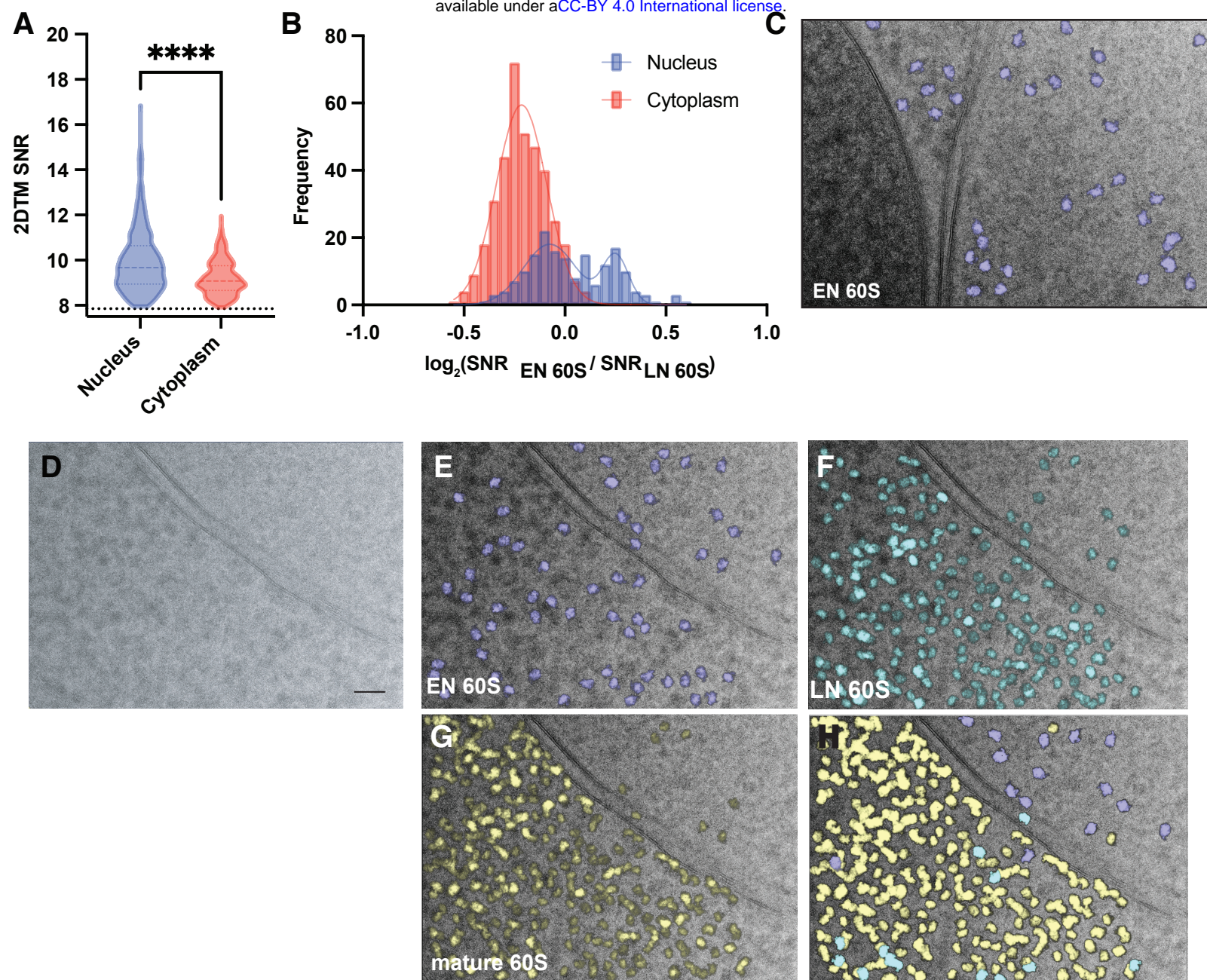


Figure 5 - figure supplement 1